

1 **Accessory Mineral Eu Anomalies in Suprasolidus Rocks: Beyond Feldspar**

2 **R. M. Holder^{1,2}, C. Yakymchuk³, and D. R. Viete²**

3 ¹Department of Earth and Environmental Sciences, University of Michigan, Ann Arbor,
4 Michigan, USA.

5 ²Department of Earth and Planetary Sciences, Johns Hopkins University, Baltimore, MD, USA.

6 ³Department of Earth and Environmental Sciences, University of Waterloo, Waterloo, ON,
7 Canada.

8 Corresponding author: Robert Holder (roholder@umich.edu)

9
10 **Key Points:**

- 11 • Eu anomalies in suprasolidus rocks record any process that changes the relative
12 availability of Eu^{2+} and Eu^{3+} , not just feldspar growth.
- 13 • Disequilibrium is required for feldspar growth to strongly influence accessory mineral Eu
14 anomalies.
- 15 • Comparing accessory mineral Eu anomalies and Sr concentrations leads to more robust
16 interpretation than evaluating Eu anomalies alone.
- 17
18

This is the author manuscript accepted for publication and has undergone full peer review but has not been through the copyediting, typesetting, pagination and proofreading process, which may lead to differences between this version and the [Version of Record](#). Please cite this article as doi: [10.1029/2020GC009052](https://doi.org/10.1029/2020GC009052)

19 **Abstract**

20 Accessory-mineral Eu anomalies (Eu/Eu^*) are routinely measured to infer changes in the amount
21 of feldspar over time, allowing accessory mineral U–Pb dates to be linked to the progressive
22 crystallization of igneous and metamorphic rocks and, by extension, geodynamic processes.
23 However, changes in Eu/Eu^* can reflect any process that changes the relative availability of Eu^{2+}
24 and Eu^{3+} . We constructed partitioning budgets for Sm, Eu^{2+} , Eu^{3+} , and Gd in suprasolidus
25 metasedimentary rocks to investigate processes that can influence accessory mineral Eu
26 anomalies. We modeled three scenarios: 1) closed-system, equilibrium crystallization; 2)
27 fractionation of Eu by feldspar growth during melt crystallization; and 3) removal of Eu by melt
28 extraction. In the closed-system equilibrium model, accessory-mineral Eu/Eu^* changes as a
29 function of $f\text{O}_2$ and monazite stability; Eu/Eu^* changes up to 0.3 over a pressure–temperature
30 range of 4–12 kbar and 700–950°C. Fractionation of Eu by feldspar growth is modeled to
31 decrease accessory-mineral Eu/Eu^* by ~0.05–0.15 per 10 wt% feldspar crystallized. Melt
32 extraction has a smaller effect; removal of 10% melt decreases accessory mineral Eu/Eu^* in the
33 residue by ≤ 0.05 . Although these models demonstrate that fractionation of Eu by feldspar growth
34 can be a dominant control on a rocks Eu budget, they also show that the common interpretation
35 that Eu/Eu^* only records feldspar growth and breakdown is an oversimplification that could lead
36 to incorrect interpretation about the duration and rates of tectonic processes. Consideration of
37 other processes that influence Eu anomalies will allow for a broader range of geological
38 processes to be investigated by petrochronology.

39 **Plain Language Summary**

40 Metamorphic rocks—rocks in which new minerals grew in response to increase in pressure and
41 temperature related to deep burial or subduction—and igneous rocks—rocks that formed as
42 magmas cool and crystallize—provide a direct record of how Earth's continents have moved and
43 changed through time. To read this record, geologists need to be able to measure the ages of
44 metamorphism and magmatism: When did it happen? How long did it last? How does it relate to
45 other rocks around the world? A common approach to addressing these questions is using U–Pb
46 dating of the minerals zircon, monazite, and apatite. The elements these minerals incorporate are
47 indicative of how hot and how deep in the Earth they were when they grew. In this paper we
48 explore how geologists can use the concentrations of the element Europium (Eu) in these
49 minerals to provide new insights into the geological significance of U–Pb dates, leading to more
50 robust interpretations of Earth's plate tectonic history.
51

52 **1 Introduction**

53 Trace-element concentrations and ratios in accessory minerals can be used to (semi-
54)quantitatively link accessory-mineral growth to the growth and breakdown of major phases (e.g.
55 Bea & Montero, 1999; Buick et al., 2006; Cioffi et al., 2019; Finger & Krenn, 2007; Foster et al.,
56 2000; Foster et al., 2002; Garber et al., 2017; Hacker et al., 2019; Hermann & Rubatto, 2003;
57 Hokada & Harley, 2004; Kelly et al., 2006; Kelly & Harley, 2005; Mottram et al., 2014; Pyle &
58 Spear, 1999; Rubatto, 2002; Rubatto & Hermann, 2007; Rubatto et al., 2006; Taylor et al., 2015;
59 Warren et al., 2019) (Figure 1). This approach—along with trace-element thermobarometers
60 (Ferry & Watson, 2007; Gratz & Heinrich, 1997; Hayden et al., 2008; Pyle et al., 2001;
61 Seydoux-Guillaume et al., 2002; Thomas et al., 2015; Tomkins et al., 2007; Wark & Watson,
62 2006) and modeling of accessory-mineral stability (Janots et al., 2007; Kelsey et al., 2008; Kohn
63 et al., 2015; Shrestha et al., 2019; Spear, 2010; Spear & Pyle, 2010; Yakymchuk, 2017;

64 Yakymchuk & Brown, 2014; Yakymchuk et al., 2017)—can be combined with *in-situ* U–Pb
65 geochronology to infer *P–T–t–d* paths of crystalline rocks that underpin interpretations of their
66 geodynamic significance (e.g. Engi, 2017; Kohn, 2017; Rubatto, 2017; Zack & Kooijman, 2017).
67 This multilayered approach to assessing the petrological and geological significance of
68 accessory-mineral U–Pb dates forms the foundation of petrochronology (Engi et al., 2017).

69 In this paper, we address one of the trace-element ratios most commonly used in
70 petrochronology: the Eu anomaly ($\text{Eu}/\text{Eu}^* = \text{Eu}_n^{\text{total}} / \sqrt{\text{Sm}_n \times \text{Gd}_n}$, subscript n denotes a
71 normalized concentration; $\text{Eu}^{\text{total}} = \text{Eu}^{3+} + \text{Eu}^{2+}$; for this paper, the normalizing values are C.I.
72 chondrite; McDonough & Sun, 1995). Variability in accessory-mineral Eu/Eu* ratios are
73 commonly attributed to the growth and breakdown of plagioclase (e.g. Holder et al., 2015) or
74 alkali-feldspar (e.g. Mottram et al., 2014; Rubatto et al., 2006; 2013; 2016); plagioclase feldspar
75 is particularly sensitive to changes in pressure and useful for investigating high pressure
76 metamorphism (e.g. O’Brien & Rötzler, 2003), whereas the modes and compositions of both
77 feldspars are sensitive to the extent of partial melting in suprasolidus rocks. However, mineral
78 Eu/Eu* might be influenced by a range of factors, including: 1) bulk-rock Eu/Eu*; 2) the
79 stability of minerals that strongly partition either Eu^{2+} or Eu^{3+} ; 3) bulk-rock $\text{Eu}^{3+}/\text{Eu}^{2+}$, which
80 depends on $f\text{O}_2$, T , and P ; 4) possible differences in the temperature-dependence of partitioning
81 for Eu^{3+} relative to Eu^{2+} ; or 5) any other process that fractionates Eu^{3+} from Eu^{2+} . Consequently,
82 accessory-mineral Eu/Eu* might not always be exclusively controlled by feldspar. The purpose
83 of this paper is to highlight the potential complexity of Eu partitioning, by modeling changes in
84 accessory-mineral Eu/Eu* for three simple, plausible scenarios (changes in $f\text{O}_2$, feldspar
85 fractionation, and open-system melting), as a basis for further discussion about interpreting
86 accessory-mineral Eu/Eu* in natural samples.

87

88 2 Methods

89 2.1 Construction of partitioning models

90 The concentrations of Sm, Eu, and Gd in accessory minerals, major minerals, and melt
91 were calculated for average suprasolidus metapelite and metagreywacke (Figure 2) as functions
92 of pressure and temperature using mineral modes and partition coefficients. Mineral modes were
93 calculated by phase-equilibrium modeling as described by Yakymchuk et al. (2017). Whole-rock
94 mass fractions of Sm, Eu, and Gd were taken to be 5.9, 1.2, and 5.2 $\mu\text{g/g}$, respectively, reflecting
95 the average values of shales (e.g. Condie, 1993). This corresponds to $\text{Eu}/\text{Eu}^*_{\text{rock}} = 0.66$.

96 There is considerable variability in the availability and quality of partitioning data. In
97 recognition of this uncertainty, models were constructed with two sets of partition coefficients,
98 referred to as “B94”—empirical partition coefficients from Bea et al. (1994)—and “modified
99 composite” (MC)—a dataset of partition coefficients compiled from multiple studies, modified
100 slightly to reduce several discrepancies observed among calculations and observations in the first
101 iterations of the model calculations (zircon and garnet: Rubatto & Hermann, 2007; Taylor et al.,
102 2015; monazite: Stepanov et al., 2012; apatite: Watson & Green, 1981; plagioclase: Sun et al.,
103 2017; alkali-feldspar: Ren, 2004). The partitioning data used in each of these models are

104 described in more detail in Texts S1 and S2 and summarized in Table 1. All partition coefficients
105 (K_d^x , x = element or ion of interest) are mineral:melt unless specifically stated.

106 The advantages of the B94 models are that: (1) The estimated peak metamorphic
107 temperature of the rocks from which the partitioning data were estimated (750°C) is lower than
108 the experimental/magmatic temperatures of most trace-element partitioning studies, and (2) The
109 rocks from which the data were estimated are similar to the modeled compositions of this study
110 (i.e. peraluminous migmatites). The B94 models do not account for the temperature- or pressure-
111 dependence of partitioning or the presence of Eu^{2+} in accessory minerals and their samples are
112 more reduced than many metasedimentary rocks (e.g. Ague, 1991; Diener & Powell, 2010;
113 Spear, 1993). The advantages of the MC models are that they account for the temperature
114 dependence of partitioning and include both Eu^{2+} and Eu^{3+} in each accessory mineral.

115 2.2 Calculating whole-rock Eu valence for partitioning models

116 The Eu species Eu^{3+} and Eu^{2+} were treated independently. Values of $K_d^{\text{Eu}^{3+}}$ were taken as
117 the geometric mean of K_d^{Sm} and K_d^{Gd} , whereas it was assumed that $K_d^{\text{Eu}^{2+}} = K_d^{\text{Sr}}$ (Philpotts,
118 1970) due to the near identical size and ionic radius of Eu^{2+} and Sr^{2+} (Shannon, 1976). We
119 assumed that the bulk-rock $\text{Eu}^{2+}/\text{Eu}^{3+}$ ratios are reasonably approximated by the equations of
120 Burnham et al. (2015), who measured Eu valence in experimental silicate melts as functions of
121 temperature, $f\text{O}_2$, and melt composition. Burnham et al. (2015) found that contours of constant
122 $\text{Eu}^{2+}/\text{Eu}^{3+}$ were parallel to the fayalite–magnetite–quartz buffer in plots of $f\text{O}_2$ vs T ,
123 demonstrating that Eu valence was controlled by Fe^{2+} – Fe^{3+} redox. This suggests that the *relative*
124 changes in Eu valence should be reasonably approximated by $f\text{O}_2$ for systems in which $f\text{O}_2$ is
125 controlled by Fe^{2+} – Fe^{3+} mineral equilibrium (among magnetite–spinel, ilmenite, biotite, and
126 garnet in our models). However, the *absolute values* of bulk-rock and mineral $\text{Eu}^{2+}/\text{Eu}^{3+}$ might
127 be different in real (semi-)pelitic systems which differ from the experiments of Burnham et al.
128 (2015) in that they are outside of their investigated compositional range (mostly mafic–
129 intermediate), at lower temperature, and they contain minerals (the experiments of Burnham et
130 al., 2015, were strictly on melts) which might impart their own crystal-chemistry influence on
131 $\text{Eu}^{2+}/\text{Eu}^{3+}$ in their structures (e.g. Philpotts, 1970). Therefore, the models should only be
132 interpreted semi-quantitatively, in terms of order-of-magnitude change and trends.

133 Models were calculated with fixed O concentrations, corresponding to slightly oxidized
134 bulk compositions ($\text{Fe}^{3+}/\text{Fe}^{\text{total}} = 0.15$; Yakymchuk et al., 2017) that produce ilmenite±magnetite
135 (e.g. Diener and Powell, 2010), consistent with observations from many natural metapelites.
136 Calculated $\log_{10}f\text{O}_2$ in the models varies between ~FMQ₊₁ and FMQ₊₃, where FMQ is the
137 fayalite–magnetite–quartz buffer and the subscript indicates logarithmic deviations from the
138 buffer. Such values are relatively common in metasedimentary granulites (e.g. Boger et al., 2012;
139 Yakymchuk et al., 2019) and typical of many lower-crustal rocks in general (Bucholz &
140 Keleman, 2019). No explicit $f\text{O}_2$ buffer was imposed on the calculations, as that would require
141 that O concentrations vary as a function of T , P , and the compositions of Fe^{2+} – Fe^{3+} solid
142 solutions to maintain the buffer (i.e. not a closed system). Values of $\text{Eu}^{3+}/\text{Eu}^{\text{total}}$ vary
143 approximately linearly over this $f\text{O}_2$ range (Burnham et al., 2015). For significantly more
144 reduced (<FMQ₋₄) or oxidized rocks (>FMQ₊₈), the equations of Burnham et al. (2015) predict
145 Eu to be monovalent: Eu^{2+} or Eu^{3+} , respectively. Our calculations are not applicable to natural

146 systems at these fO_2 extremes (such as graphite–pyrite-bearing metapelites; Connolly & Cesare,
147 1993).

148 2.3 Model scenarios

149 (1) In the equilibrium closed-system partitioning models, partition coefficients were used
150 to calculate concentrations of Sm, Eu, and Gd in each relevant mineral as functions of mineral
151 modes, temperature, and Eu^{2+}/Eu^{3+} ratio. (2) The models of Eu fractionation by feldspar
152 crystallization were calculated along an isobaric cooling path at 6 kbar. The models began at
153 950°C with REE-equilibrium among all phases. The REE incorporated into plagioclase and
154 alkali-feldspar as they grew was incrementally removed from the effective whole-rock
155 composition at one-degree-K cooling intervals. All other aspects of these models were assumed
156 to be in equilibrium (e.g. mineral modes, major-element compositions, and REE partitioning
157 among all other phases) to specifically isolate the influence of feldspar fractionation on
158 accessory mineral Eu anomalies. For portions of the modeled cooling path in which the mode of
159 either plagioclase or alkali-feldspar decreased, a proportionate amount of the previously
160 fractionated REE was added back into the effective bulk-composition. (3) For the models of melt
161 extraction during isobaric heating, REE equilibrium was maintained among all phases. When the
162 melt fraction reached 7 mol%, approximately the melt-connectivity threshold (Rosenberg &
163 Handy, 2005), the major-element equivalent of 6 mol% melt was removed from the model
164 composition (leaving 1% remaining) along with proportionate amounts of Sm, Eu, and Gd.
165 Although the exact value of this melt-connectivity threshold will depend on grain size, grain
166 shape, and deformation, this approach is used for consistency with the now-common melt-
167 reintegration method used by Korhonen et al. (2013) to estimate the protolith composition of
168 residual granulites (this approach is the inverse of theirs). The weight fractions of accessory
169 minerals were also modified by each melt-extraction step in accordance with their solubilities
170 (e.g. Yakymchuk, 2017).

171 3 Results

172 Results of the models are tabulated in Data Sets S1–S16, which are available through the
173 EarthChem community data repository (Holder et al., 2020).

174 3.1 Models of equilibrium, unbuffered, closed-system metamorphism

175 Contours of oxygen fugacity ($\log_{10}fO_2$), oxygen fugacity relative to the fayalite–
176 magnetite–quartz buffer ($\log_{10}fO_{2\text{ rock}} - \log_{10}fO_{2\text{ FMQ}}$), and Eu valence ($Eu^{3+}/Eu^{\text{total}}$) as functions
177 of pressure and temperature are shown in Figure 3. Contours of $\log_{10}fO_{2\text{ rock}} - \log_{10}fO_{2\text{ FMQ}}$
178 (Figure 3c,d) parallel reactions among the Fe^{2+} – Fe^{3+} minerals (ilmenite, magnetite–spinel,
179 garnet, and biotite). At higher pressure, the contours closely parallel the rutile-in reaction, which
180 involves breakdown of ilmenite to form garnet and rutile with increasing pressure; the slope of
181 this reaction changes between 750 and 850°C due to the breakdown of biotite. At lower pressure,
182 the contours become more closely spaced, following magnetite–spinel stability, with a notable
183 “trough” at ~750°C.

184 Contours of $Eu^{3+}/Eu^{\text{total}}$ (Figure 3e,f) are similar to the contours of $\log_{10}fO_{2\text{ rock}} - \log_{10}fO_{2\text{ FMQ}}$
185 (Figure 3c,d), as expected from the Fe-redox-controlled Eu-redox equations used in the

186 models (Burnham et al., 2015). The overall changes in $\text{Eu}^{3+}/\text{Eu}^{\text{total}}$ across the models (675–
187 950°C, 4–12 kbar) is 0.2–0.3 in both pelite and greywacke. The values of $\text{Eu}^{3+}/\text{Eu}^{\text{total}}$ are
188 primarily functions of pressure, due to the pressure-dependence of oxide stability, with slight
189 deflection associated with biotite breakdown, as mentioned in the previous paragraph.

190 Calculated Eu/Eu^* in the accessory minerals and garnet in the MC models are shown in
191 Figure 4. The values for each mineral are ~ 0.6 – 0.7 at higher pressure and 0.4 – 0.5 at lower
192 pressure. At lower temperature, where all three accessory minerals are abundant, the contours of
193 Eu/Eu^* essentially parallel the contours of whole-rock $\text{Eu}^{3+}/\text{Eu}^{\text{total}}$ (Figure 3e,f). However, at
194 $\sim 850^\circ\text{C}$ (pelite) and $\sim 900^\circ\text{C}$ (greywacke), contours of Eu/Eu^* are more temperature-dependent;
195 this change occurs as the mode of monazite decreases exponentially, until it is not stable. For the
196 B94 models, accessory-mineral Eu/Eu^* parallels whole-rock $\text{Eu}^{3+}/\text{Eu}^{\text{total}}$ (Figure S1), because
197 accessory-mineral $K_d^{\text{Eu}^{2+}} = 0$. Calculated Eu/Eu^* anomalies of plagioclase and melt in the MC
198 model are shown in Figure 5. Values of Eu/Eu^* in feldspars and melt decrease with increasing
199 temperature and show little pressure dependence, except for the B94 greywacke model (Figure
200 S2) in which plagioclase and melt Eu/Eu^* show a stronger pressure dependence near the solidus.

201 Figure 6 shows the proportion of each phase, their total Eu content, and their Eu/Eu^*
202 from the MC models along a hypothetical clockwise P – T path consisting of isobaric heating at
203 10 kbar to 850°C , isothermal decompression at 850°C to 5 kbar, and isobaric cooling at 5 kbar to
204 675°C . As described above, feldspars and melt Eu/Eu^* changes most significantly with
205 temperature, whereas Eu/Eu^* of the accessory minerals and garnet ($K_d^{\text{Eu}^{3+}} \gg K_d^{\text{Eu}^{2+}}$) change
206 most significantly with pressure. The total change in accessory mineral Eu/Eu^* along such a P – T
207 path is similar in all models: approximately -0.1 to -0.2 . Pressure–temperature paths that pass
208 through lower pressure and higher temperature conditions, where magnetite–spinel is stable,
209 would result in slightly larger changes in Eu/Eu^* for the accessory minerals and garnet (Figure
210 3e,f; e.g. Holder et al., 2018).

211 Figure 7 shows apatite Eu/Eu^* as functions of T , P , feldspar wt%, and $\text{Eu}^{3+}/\text{Eu}^{\text{total}}$ on
212 accessory mineral Eu/Eu^* in the closed-system, equilibrium MC models. Apatite is plotted,
213 because it exhibits the largest P – T stability range of the accessory minerals; however, monazite
214 and zircon exhibit similar relationships (Figures 4, 6). Viewed together, these plots illustrate that
215 the relationship of accessory mineral Eu/Eu^* with feldspar is nonsystematic. In contrast, changes
216 in pressure and temperature show strong consistent effects, due to changes in bulk-rock Eu
217 valence (changes in $f\text{O}_2$, relative to the FMQ buffer) and monazite stability, respectively. Total
218 changes in accessory mineral Eu/Eu^* over the modeled P – T conditions are 0.2–0.3.

219 3.2 Models of feldspar fractionation

220 Figure 8 shows the results of the models in which REE are fractionated by feldspars
221 during isobaric cooling and melt crystallization. Models were stopped when the weight fractions
222 of the feldspars became essentially constant, making the fractionation calculations non-
223 applicable. For the pelite model, this occurred at 700°C , slightly above the calculated solidus.
224 For linguistic simplicity, we refer to 700°C as “the solidus” for the pelite models in the following

225 paragraphs. For the greywacke model, the weight fractions of feldspar are essentially constant at
226 $T < 798^{\circ}\text{C}$.

227 In all models, the effective whole-rock Eu/Eu^* decreases with cooling, as the amount of
228 feldspar increases. In the MC pelite model, the significant resorption of alkali-feldspar as biotite
229 begins to crystallize (at 813°C) results in a sharp increase in effective whole-rock Eu/Eu^* , before
230 continued plagioclase crystallization draws the value back down. The B94 pelite model does not
231 show the same influence of the biotite-in reaction, due to much lower values of $K_d^{\text{Eu}^{2+}}$ in the
232 alkali feldspar. Values of Eu/Eu^* in accessory minerals and garnet are generally sub-parallel to
233 the whole-rock values, with deviations due to changes in mineral modes and differences in $K_d^{\text{Eu}^{3+}}$
234 and $K_d^{\text{Eu}^{2+}}$ among minerals.

235 3.3 Models of melt extraction

236 Figure 9 shows the results of models in which REE were removed by step-wise melt
237 extraction during isobaric heating based on their equilibrium values in melt. The results of the
238 calculations differ substantially between the MC and B94 models.

239 For the MC models, melt extraction changes the bulk-rock Eu/Eu^* very little from the
240 initial value of 0.66. Accessory-mineral and garnet Eu/Eu^* show a total variability of 0.10–0.15
241 (pelite) and ~ 0.02 (greywacke). The greywacke models show less variability in Eu/Eu^* , because
242 less melt is produced and extracted. For the B94 models, melt extraction changes the bulk-rock
243 Eu/Eu^* more appreciably than in the MC models. Bulk-rock Eu/Eu^* decreases from 0.66 to 0.53
244 (pelite) or 0.63 (greywacke). Values of accessory-mineral and garnet Eu/Eu^* generally follow
245 the effective whole-rock Eu/Eu^* , decreasing as melt is extracted.

246 The differences between results of the MC and B94 melt-extraction models are primarily
247 due to differences in the calculated Eu/Eu^* of the melt. In the B94 models, the Eu/Eu^* of the
248 melt is 14 (greywacke) or 18 (pelite) at the solidus and remains greater than unity for most of the
249 models, allowing for substantial removal of Eu relative to other REE during melt extraction. In
250 the MC models, the Eu/Eu^* of the melt is 2.4 (greywacke) or 4.5 (pelite) at the solidus and
251 decreases below unity at 876°C (greywacke) or 830°C (pelite); although melt was extracted
252 multiple times within this temperature range, the draw-down in whole-rock Eu/Eu^* is negligible
253 due to the relatively low Eu/Eu^* and low total concentrations of REE in the melt.

254 4 Discussion

255 4.1 Controls on equilibrium mineral Eu/Eu^*

256 Interpreting Eu/Eu^* in minerals is complicated by presence of both Eu^{2+} and Eu^{3+} in most
257 metamorphic and igneous environments. The equilibrium Sm–Eu–Gd partitioning calculations
258 shown in Figures 3–7 provide a starting point to understand the processes that control mineral
259 Eu/Eu^* .

260 Both feldspars and melt preferentially incorporate Eu^{2+} over Eu^{3+} , resulting in Eu/Eu^*
261 consistently greater than the whole-rock value. However, in all models, the values of feldspar
262 and melt Eu/Eu^* decrease by approximately an order of magnitude from 700 to 950°C (Figure
263 5). This is due to several effects: 1) temperature- and composition-dependence of feldspar K_d 's

264 (e.g. plagioclase $K_d^{\text{Eu}^{2+}}$ decreases from 8.4 to 0.33 between 700 to 950°C at 10 kbar in the MC
265 pelite model); 2) increase in the proportion of melt (Eu^{2+} must be shared among feldspars and
266 melt); and 3) dissolution of accessory minerals, most prominently monazite (Figure 6, 7), which
267 requires that their Sm, Gd, and Eu (mostly Eu^{3+}) must be redistributed among the other phases.

268 The accessory minerals and garnet have very large $\text{Eu}^{3+}/\text{Eu}^{2+}$ ratios (>10–100). Values of
269 Eu/Eu^* in these minerals is primarily controlled by the availability of Eu^{3+} . Contours of
270 accessory mineral Eu/Eu^* (Figure 4) are sub-parallel to the whole-rock $\text{Eu}^{3+}/\text{Eu}^{\text{total}}$ contours
271 (Figure 3e,f), which is governed by $f\text{O}_2$ (in the B94 models, this is the only control). An
272 exception to this is: at ~850°C (pelite) and ~900°C (greywacke), the amount of monazite
273 decreases exponentially until it becomes fully dissolved in the melt (Figure 4), causing the
274 accessory-mineral Eu/Eu^* contours to deviate from the whole-rock $\text{Eu}^{3+}/\text{Eu}^{\text{total}}$ contours.

275 Most importantly for this study, in the equilibrium closed-system models, there is no
276 systematic correlation between feldspar abundance and accessory mineral Eu/Eu^* . Apparent
277 correlations occur for some P – T conditions, but these vary in sign and magnitude (Figure 7a,b)
278 and are more appropriately attributed to changes in pressure and temperature, which influence
279 modeled $\text{Eu}^{3+}/\text{Eu}^{\text{total}}$ and the mode of monazite, respectively (Figure 7c,d). This lack of a clear
280 relationship with the amount of feldspar is expected, because feldspars and accessory minerals
281 are mostly competing for different species of Eu (Eu^{2+} and Eu^{3+} , respectively; e.g. Kohn and
282 Kelly, 2017). Maximum changes in equilibrium accessory-mineral Eu/Eu^* are predicted to be
283 ~0.2–0.3 for the modeled suprasolidus conditions. Due to the strong pressure dependence of
284 accessory-mineral Eu/Eu^* in the models, clockwise P – T paths are predicted to result in a net
285 decrease in Eu/Eu^* , whereas counter-clockwise paths are predicted to result in a net increase in
286 Eu/Eu^* .

287 4.2 Open system effects on mineral Eu/Eu^*

288 4.2.1 Fractionation of Eu by feldspar crystallization

289 The calculations shown in Figure 8 support the hypothesis that feldspar growth and
290 breakdown can significantly influence accessory mineral Eu/Eu^* if the REE incorporated into
291 feldspar are effectively fractionated from the rest of the rock. For the MC models, crystallization
292 of 10% feldspar resulted in a decrease in accessory mineral Eu/Eu^* of ~0.15, with a maximum
293 possible decrease of ~0.4; for the B94 models, the corresponding decrease was smaller but not
294 insignificant: ~0.05 for 10% feldspar crystallization, with a maximum possible decrease of
295 ~0.15. However, application of these generalizations to real rocks is complicated by the
296 recognition that alkali-feldspar and plagioclase modes are unlikely to change monotonically
297 during crystallization; they grow/breakdown as functions of their miscibility, and due to
298 reactions with garnet (such as the “GASP” reaction), incongruent versus congruent melting, melt
299 crystallization and reactions with micas. For example, the MC pelite model (Figure 8c) shows
300 accessory mineral Eu/Eu^* with increases and decreases of > 0.1 during cooling as a result of
301 feldspar crystallization at high temperature then feldspar resorption and mica crystallization at
302 lower temperature. Another complication is that Eu^{2+} diffusivity in feldspar, if similar to Sr
303 diffusivity, is ~4 orders of magnitude higher than REE^{3+} diffusivity (Cherniak 1995, Cherniak &
304 Watson, 1992; Cherniak & Watson, 1994); fractionation of Eu by feldspar growth might
305 therefore be limited at suprasolidus conditions. Nevertheless, the very large changes in accessory

306 mineral Eu/Eu* observed in some samples (≥ 0.4 , Figure 1; e.g. Rubatto et al., 2006), likely
307 require some degree of Eu fractionation by feldspar growth.

308 4.2.2 Open-system melting

309 In our models, melt Eu/Eu* was greater than whole-rock Eu/Eu* at all conditions.
310 Therefore, extraction of melt from migmatites has the potential to decrease whole-rock Eu/Eu*,
311 but the modeled magnitude of this decrease depends on the partitioning data used. Observations
312 of leucosome:melanosome trace-element ratios in natural samples from Bea et al. (1994) suggest
313 that partial melt extraction can have a substantial influence on Eu/Eu* in residual minerals
314 (Eu/Eu* changes > 0.1 in the B94 models; Figure 8). However, the MC models suggest that
315 open-system melting will have essentially no influence on accessory-mineral Eu/Eu*. It is
316 possible that the discrepancy in these results relates to how the partitioning data for the two
317 models were estimated. The partitioning data of Bea et al. (1994) are based on
318 mineral:leucosome trace-element ratios; however, leucosomes rarely record initial melt
319 compositions, due to fractional crystallization of feldspar (physical separation of feldspar from
320 residual melt as the leucosome crystallizes: e.g. Brown et al., 2016; Sawyer, 1987).
321 Consequently, the B94 models might have overpredicted the concentration of Eu²⁺ and Eu/Eu*
322 in the melt.

323 5 Conclusions

324 As hypothesized by Rubatto et al. (2006), our models predict that growth of feldspar can
325 significantly influence accessory-mineral Eu/Eu*, but only if REE in feldspar are effectively
326 fractionated from the rock. At equilibrium, the mode of feldspar has negligible/subordinate
327 effects on accessory-mineral Eu/Eu* compared to fO_2 and the stability of monazite (for the
328 suprasolidus peraluminous rocks modeled). Feldspars do not strongly influence accessory-
329 mineral Eu/Eu* at equilibrium, because feldspars and accessory minerals predominantly
330 incorporate different Eu species (Eu²⁺ and Eu³⁺, respectively; e.g. Kohn & Kelly, 2017).

331 Whereas Y+HREE partitioning among accessory minerals and garnet is relatively well
332 understood (e.g. Pyle et al., 2001), Eu partitioning is highly complex. This makes interpretation
333 of Eu/Eu* more difficult than Y+HREE, but might allow for a broader range of geological
334 processes to be investigated with petrochronology, particularly open-system processes such as
335 fluid–rock interaction, partial melting, and magma crystallization. The models presented here
336 provide a basis for further study, but are limited in application to suprasolidus peraluminous
337 rocks. The models are also limited in theory by available partitioning data and a lack of
338 quantification on the crystal chemical effects on Eu valence in minerals. To fully understand
339 accessory mineral Eu/Eu*, the roles of other minerals (e.g. allanite, amphibole, titanite in
340 metabasites and intermediate rocks) also needs to be assessed. In addition, systematic
341 assessments of Eu/Eu* in natural samples, as have been undertaken for mineral Y+HREE
342 concentrations, are needed (e.g. Bea & Montero, 1999; Foster et al., 2000; Hermann & Rubatto,
343 2003; Pyle & Spear, 1999).

344

345 **Acknowledgments**

346 This work was supported by the Morton K Blaustein Department of Earth and Planetary
347 Sciences, Johns Hopkins University. The authors declare no conflicts of interest. Tabulated
348 results of the models in this paper can be found in the EarthChem community data repository,
349 DOI: 10.26022/IEDA/111590. Author contributions following the CRediT taxonomy: Holder:
350 conceptualization, data curation, formal analysis, methodology, visualization, writing – original
351 draft; Yakymchuk: formal analysis, methodology, writing – review & editing; Viète: funding
352 acquisition, resources, visualization, writing – review & editing. The authors thank Miguel
353 Cisneros and Pierre Lanari for their helpful reviews, which improved the presentation and
354 discussion of this work.

355 **References**

- 356 Ague, J. J. (1991). Evidence for major mass transfer and volume strain during regional metamorphism of pelites.
357 *Geology*, 19(8), 855–858. [https://doi.org/10.1130/0091-7613\(1991\)019<0855:EFMMTA>2.3.CO;2](https://doi.org/10.1130/0091-7613(1991)019<0855:EFMMTA>2.3.CO;2)
- 358 Bea, F., & Montero, P. (1999). Behavior of accessory phases and redistribution of Zr, REE, Y, Th, and U during
359 metamorphism and partial melting of metapelites in the lower crust : An example from the Kinzigite
360 Formation of Ivrea-Verbano , NW Italy. *Geochimica et Cosmochimica Acta*, 63(7/8), 1133–1153.
361 <https://doi.org/10.1016/S0016-7037>
- 362 Boger, S. D., White, R. W., & Schulte, B. (2012). The importance of iron speciation (Fe²⁺/Fe³⁺) in determining
363 mineral assemblages: an example from the high-grade aluminous metapelites of southeastern Madagascar.
364 *Journal of Metamorphic Geology*, 30(9), 997–1018. <https://doi.org/10.1111/jmg.12001>
- 365 Brown, C. R., Yakymchuk, C., Brown, M., Fanning, C. M., Korhonen, F. J., Piccoli, P. M., & Siddoway, C. S.
366 (2016). From source to sink: Petrogenesis of cretaceous anatectic granites from the Fosdick migmatite-granite
367 complex, West Antarctica. *Journal of Petrology*, 57(7), 1241–1278. <https://doi.org/10.1093/petrology/egw039>
- 368 Bucholz, C. E., & Kelemen, P. B. (2019). Oxygen fugacity at the base of the Talkeetna arc, Alaska. *Contributions to*
369 *Mineralogy and Petrology*, 174(10), 1–27. <https://doi.org/10.1007/s00410-019-1609-z>
- 370 Buick, I. S., Hermann, J., Williams, I. S., Gibson, R. L., & Rubatto, D. (2006). A SHRIMP U–Pb and LA-ICP-MS
371 trace element study of the petrogenesis of garnet–cordierite–orthoamphibole gneisses from the Central Zone
372 of the Limpopo Belt, South Africa. *Lithos*, 88(1–4), 150–172. <https://doi.org/10.1016/j.lithos.2005.09.001>
- 373 Burnham, A. D., Berry, A. J., Halse, H. R., Schofield, P. F., Cibin, G., & Mosselmans, J. F. W. (2015). The
374 oxidation state of europium in silicate melts as a function of oxygen fugacity, composition and temperature.
375 *Chemical Geology*, 411, 248–259. <https://doi.org/10.1016/j.chemgeo.2015.07.002>
- 376 Cherniak, D. J. (2003). REE diffusion in feldspar. *Chemical Geology*, 193(1–2), 25–41.
377 [https://doi.org/10.1016/S0009-2541\(02\)00246-2](https://doi.org/10.1016/S0009-2541(02)00246-2)
- 378 Cherniak, D. J., & Watson, E. B. (1992). A study of strontium diffusion in K-feldspar, Na-K feldspar and anorthite
379 using Rutherford Backscattering Spectroscopy. *Earth and Planetary Science Letters*, 113(3), 411–425.
380 [https://doi.org/10.1016/0012-821X\(92\)90142-I](https://doi.org/10.1016/0012-821X(92)90142-I)
- 381 Cherniak, D. J., & Watson, E. B. (1994). A study of strontium diffusion in plagioclase using Rutherford
382 backscattering spectroscopy. *Geochimica et Cosmochimica Acta*, 58(23), 5179–5190.

383 [https://doi.org/10.1016/0016-7037\(94\)90303-4](https://doi.org/10.1016/0016-7037(94)90303-4)

384 Cioffi, C. R., Campos Neto, M. da C., Möller, A., & Rocha, B. C. (2019). Titanite petrochronology of the southern
385 Brasília Orogen basement: Effects of retrograde net-transfer reactions on titanite trace element compositions.
386 *Lithos*, 344–345, 393–408. <https://doi.org/10.1016/j.lithos.2019.06.035>

387 Condie, K. C. (1993). Chemical composition and evolution of the upper continental crust: Contrasting results from
388 surface samples and shales. *Chemical Geology*, 104(1–4), 1–37. [https://doi.org/10.1016/0009-2541\(93\)90140-](https://doi.org/10.1016/0009-2541(93)90140-E)
389 E

390 Connolly, J. A. D., & Cesare, B. (1993). C-O-H-S fluid composition and oxygen fugacity in graphitic metapelites.
391 *Journal of Metamorphic Geology*, 11(3), 379–388. <https://doi.org/10.1111/j.1525-1314.1993.tb00155.x>

392 Diener, J. F. A., & Powell, R. (2010). Influence of ferric iron on the stability of mineral assemblages. *Journal of*
393 *Metamorphic Geology*, 28(6), 599–613. <https://doi.org/10.1111/j.1525-1314.2010.00880.x>

394 Engi, M. (2017). Petrochronology Based on REE-Minerals: Monazite, Allanite, Xenotime, Apatite. *Reviews in*
395 *Mineralogy and Geochemistry*, 83(1), 365 LP – 418. <https://doi.org/10.2138/rmg.2017.83.12>

396 Engi, M., Lanari, P., & Kohn, M. J. (2017). Significant Ages—An Introduction to Petrochronology. *Reviews in*
397 *Mineralogy and Geochemistry*, 83(1), 1–12. <https://doi.org/10.2138/rmg.2017.83.1>

398 Ferry, J. M., & Watson, E. B. (2007). New thermodynamic models and revised calibrations for the Ti-in-zircon and
399 Zr-in-rutile thermometers. *Contributions to Mineralogy and Petrology*, 154(4), 429–437.
400 <https://doi.org/10.1007/s00410-007-0201-0>

401 Finger, F., & Krenn, E. (2007). Three metamorphic monazite generations in a high-pressure rock from the
402 Bohemian Massif and the potentially important role of apatite in stimulating polyphase monazite growth along
403 a PT loop. *Lithos*, 95(1–2), 103–115. <https://doi.org/10.1016/j.lithos.2006.06.003>

404 Foster, G., Kinny, P., Vance, D., Prince, C., & Harris, N. (2000). The significance of monazite U–Th–Pb age data in
405 metamorphic assemblages; a combined study of monazite and garnet chronometry. *Earth and Planetary*
406 *Science Letters*, 181(3), 327–340. [https://doi.org/10.1016/S0012-821X\(00\)00212-0](https://doi.org/10.1016/S0012-821X(00)00212-0)

407 Foster, G., Gibson, H. D., Parrish, R., Horstwood, M., Fraser, J., & Tindle, A. (2002). Textural, chemical and
408 isotopic insights into the nature and behaviour of metamorphic monazite. *Chemical Geology*, 191(1–3), 183–
409 207. [https://doi.org/10.1016/S0009-2541\(02\)00156-0](https://doi.org/10.1016/S0009-2541(02)00156-0)

410 Garber, J. M., Hacker, B. R., Kylander-Clark, A. R. C., Stearns, M. A., & Seward, G. (2017). Controls on trace
411 element uptake in metamorphic titanite: Implications for petrochronology. *Journal of Petrology*, 58(6), 1031–
412 1057. <https://doi.org/10.1093/petrology/egx046>

413 Gratz, R., & Heinrich, W. (1997). Monazite-xenotime thermobarometry: Experimental calibration of the miscibility
414 gap in the binary system CePO₄-YPO₄. *American Mineralogist*, 82(7–8), 772–780.

415 Hacker, B., Kylander-Clark, A., & Holder, R. (2019). REE partitioning between monazite and garnet: Implications
416 for petrochronology. *Journal of Metamorphic Geology*, 37(2), 227–237. <https://doi.org/10.1111/jmg.12458>

417 Hayden, L. A., Watson, E. B., & Wark, D. A. (2008). A thermobarometer for sphene (titanite). *Contributions to*
418 *Mineralogy and Petrology*, 155(4), 529–540. <https://doi.org/10.1007/s00410-007-0256-y>

419 Hermann, J., & Rubatto, D. (2003). Relating zircon and monazite domains to garnet growth zones: age and duration

420 of granulite facies metamorphism in the Val Malenco lower crust. *Journal of Metamorphic Geology*, 21(9),
421 833–852. <https://doi.org/10.1046/j.1525-1314.2003.00484.x>

422 Hokada, T., & Harley, S. L. (2004). Zircon growth in UHT leucosome: Constraints from zircon-garnet rare earth
423 elements (REE) relations in Napier Complex, East Antarctica. *Journal of Mineralogical and Petrological
424 Sciences*, 99(4), 180–190. <https://doi.org/10.2465/jmps.99.180>

425 Holder, R. M., Hacker, B. R., Horton, F., & Rakotondrazafy, A. F. M. (2018). Ultrahigh-temperature osumilite
426 gneisses in southern Madagascar record combined heat advection and high rates of radiogenic heat production
427 in a long-lived high- T orogen. *Journal of Metamorphic Geology*, 36(7), 855–880.
428 <https://doi.org/10.1111/jmg.12316>

429 Holder, R. M., Hacker, B. R., Kylander-Clark, A. R. C., & Cottle, J. M. (2015). Monazite trace-element and isotopic
430 signatures of (ultra)high-pressure metamorphism: Examples from the Western Gneiss Region, Norway.
431 *Chemical Geology*, 409, 99–111. <https://doi.org/10.1016/j.chemgeo.2015.04.021>

432 Holder, R., Yakymchuk, C., Viete, D. (2020). Modeled mineral Eu anomalies in suprasolidus metasediments,
433 Version 1.0. Interdisciplinary Earth Data Alliance (IEDA). <https://doi.org/10.26022/IEDA/111590>

434 Janots, E., Brunet, F., Goffé, B., Poinssot, C., Burchard, M., & Cemič, L. (2007). Thermochemistry of monazite-
435 (La) and dissakisite-(La): Implications for monazite and allanite stability in metapelites. *Contributions to
436 Mineralogy and Petrology*, 154(1), 1–14. <https://doi.org/10.1007/s00410-006-0176-2>

437 Kelly, N. M., Clarke, G. L., & Harley, S. L. (2006). Monazite behaviour and age significance in poly-metamorphic
438 high-grade terrains: A case study from the western Musgrave Block, central Australia11Abbreviations: After
439 Kretz, 1983. *Lithos*, 88(1–4), 100–134. <https://doi.org/10.1016/j.lithos.2005.08.007>

440 Kelly, N. M., & Harley, S. L. (2005). An integrated microtextural and chemical approach to zircon geochronology:
441 Refining the Archaean history of the Napier Complex, east Antarctica. *Contributions to Mineralogy and
442 Petrology*, 149(1), 57–84. <https://doi.org/10.1007/s00410-004-0635-6>

443 Kelsey, D. E., Clark, C., & Hand, M. (2008). Thermobarometric modelling of zircon and monazite growth in melt-
444 bearing systems: examples using model metapelitic and metapsammitic granulites. *Journal of Metamorphic
445 Geology*, 26(2), 199–212. <https://doi.org/10.1111/j.1525-1314.2007.00757.x>

446 Kohn, M. J. (2017). Titanite Petrochronology. *Reviews in Mineralogy and Geochemistry*, 83.
447 <https://doi.org/10.2138/rmg.2017.83.13>

448 Kohn, M. J., Corrie, S. L., & Markley, C. (2015). The fall and rise of metamorphic zircon. *American Mineralogist*,
449 100(4), 897–908. <https://doi.org/10.2138/am-2015-5064>

450 Kohn, M. J., & Kelly, N. M. (2017). Petrology and geochronology of metamorphic zircon. *Microstructural
451 Geochronology: Planetary Records Down to Atom Scale*, 35–61. <https://doi.org/10.1002/9781119227250.ch2>

452 Korhonen, F. J., Brown, M., Clark, C., & Bhattacharya, S. (2013). Osumilite-melt interactions in ultrahigh
453 temperature granulites: Phase equilibria modelling and implications for the P-T-t evolution of the eastern ghats
454 province, India. *Journal of Metamorphic Geology*, 31(8), 881–907. <https://doi.org/10.1111/jmg.12049>

455 Mottram, C. M., Warren, C. J., Regis, D., Roberts, N. M. W., Harris, N. B. W., Argles, T. W., & Parrish, R. R.
456 (2014). Developing an inverted barrovian sequence; insights from monazite petrochronology. *Earth and*

457 *Planetary Science Letters*, 403, 418–431. <https://doi.org/10.1016/j.epsl.2014.07.006>

458 O'Brien, P. J., & Rötzler, J. (2003). High-pressure granulites: Formation, recovery of peak conditions and
459 implications for tectonics. *Journal of Metamorphic Geology*, 21(1), 3–20. [https://doi.org/10.1046/j.1525-](https://doi.org/10.1046/j.1525-1314.2003.00420.x)
460 1314.2003.00420.x

461 Philpotts, J. A. (1970). Redox estimation from a calculation of Eu²⁺ and Eu³⁺ concentrations in natural phases.
462 *Earth and Planetary Science Letters*, 9(3), 257–268. [https://doi.org/10.1016/0012-821X\(70\)90036-1](https://doi.org/10.1016/0012-821X(70)90036-1)

463 Pyle, J. M., & Spear, F. S. (1999). Yttrium zoning in garnet: Coupling of major and accessory phases during
464 metamorphic reactions. *Geological Materials Research*, 1(6), 1–49.

465 Pyle, J. M., Spear, F. S., Rudnick, R. L., & McDonough, W. F. (2001). Monazite–Xenotime–Garnet Equilibrium in
466 Metapelites and a New Monazite–Garnet Thermometer. *Journal of Petrology*, 42(11), 2083–2107.
467 <https://doi.org/10.1093/petrology/42.11.2083>

468 Ren, M. (2004). Partitioning of Sr, Ba, Rb, Y, and LREE between alkali feldspar and peraluminous silicic magma.
469 *American Mineralogist*, 89(8–9), 1290–1303. <https://doi.org/10.2138/am-2004-8-918>

470 Rosenberg, C. L., & Handy, M. R. (2005). Experimental deformation of partially melted granite revisited:
471 Implications for the continental crust. *Journal of Metamorphic Geology*, 23(1), 19–28.
472 <https://doi.org/10.1111/j.1525-1314.2005.00555.x>

473 Rubatto, D. (2002). Zircon trace element geochemistry: distribution coefficients and the link between U–Pb ages and
474 metamorphism. *Chemical Geology*, 184, 123–138. Retrieved from www.elsevier.com/locate/chemgeo

475 Rubatto, D. (2017). Zircon: The Metamorphic Mineral. *Reviews in Mineralogy and Geochemistry*, 83(1), 261 LP –
476 295. <https://doi.org/10.2138/rmg.2017.83.10>

477 Rubatto, D., Chakraborty, S., & Dasgupta, S. (2013). Timescales of crustal melting in the Higher Himalayan
478 Crystallines (Sikkim, Eastern Himalaya) inferred from trace element-constrained monazite and zircon
479 chronology. *Contributions to Mineralogy and Petrology*, 165(2), 349–372. [https://doi.org/10.1007/s00410-](https://doi.org/10.1007/s00410-012-0812-y)
480 012-0812-y

481 Rubatto, D., & Hermann, J. (2007). Experimental zircon/melt and zircon/garnet trace element partitioning and
482 implications for the geochronology of crustal rocks. *Chemical Geology*, 241(1–2), 38–61.
483 <https://doi.org/10.1016/j.chemgeo.2007.01.027>

484 Rubatto, D., Hermann, J., & Buick, I. S. (2006). Temperature and Bulk Composition Control on the Growth of
485 Monazite and Zircon During Low-pressure Anatexis (Mount Stafford, Central Australia). *Journal of*
486 *Petrology*, 47(10), 1973–1996. <https://doi.org/10.1093/petrology/egl033>

487 Sawyer, E. W. (1987). The role of partial melting and fractional crystallization in determining discordant migmatite
488 leucosome compositions. *Journal of Petrology*, 28(3), 445–473. <https://doi.org/10.1093/petrology/28.3.445>

489 Seydoux-Guillaume, A.-M., Wirth, R., Heinrich, W., & Montel, J.-M. (2002). Experimental determination of
490 Thorium partitioning between monazite and xenotime using analytical electron microscopy and X-ray
491 diffraction Rietveld analysis. *European Journal of Mineralogy*, 14(5), 869–878. [https://doi.org/10.1127/0935-](https://doi.org/10.1127/0935-1221/2002/0014-0869)
492 1221/2002/0014-0869

493 Shannon, R. D. (1976). Revised Effective Ionic Radii and Systematic Studies of Interatomic Distances in Halides

494 and Chalcogenides. *Acta Crystallographica*, *A32*, 751–767.

495 Shrestha, S., Larson, K. P., Duesterhoeft, E., Soret, M., & Cottle, J. M. (2019). Thermodynamic modelling of
496 phosphate minerals and its implications for the development of P-T-t histories: A case study in garnet -
497 monazite bearing metapelites. *Lithos*, *334–335*, 141–160. <https://doi.org/10.1016/j.lithos.2019.03.021>

498 Spear, Frank S. (1993). *Metamorphic phase equilibria and pressure-temperature-time paths*. Monograph /
499 Mineralogical Society of America. Washington, D.C.: Mineralogical Society of America.

500 Spear, F. S. (2010). Monazite–allanite phase relations in metapelites. *Chemical Geology*, *279*(1–2), 55–62.
501 <https://doi.org/10.1016/j.chemgeo.2010.10.004>

502 Spear, F. S., & Pyle, J. M. (2010). Theoretical modeling of monazite growth in a low-Ca metapelite. *Chemical*
503 *Geology*, *273*(1–2), 111–119. <https://doi.org/10.1016/j.chemgeo.2010.02.016>

504 Stepanov, A. S., Hermann, J., Rubatto, D., & Rapp, R. P. (2012). Experimental study of monazite/melt partitioning
505 with implications for the REE, Th and U geochemistry of crustal rocks. *Chemical Geology*, *300–301*, 200–
506 220. <https://doi.org/10.1016/j.chemgeo.2012.01.007>

507 Sun, C., Graff, M., & Liang, Y. (2017). Trace element partitioning between plagioclase and silicate melt: The
508 importance of temperature and plagioclase composition, with implications for terrestrial and lunar magmatism.
509 *Geochimica et Cosmochimica Acta*, *206*, 273–295. <https://doi.org/10.1016/j.gca.2017.03.003>

510 Taylor, R. J. M., Harley, S. L., Hinton, R. W., Elphick, S., Clark, C., & Kelly, N. M. (2015). Experimental
511 determination of REE partition coefficients between zircon, garnet and melt: A key to understanding high-T
512 crustal processes. *Journal of Metamorphic Geology*, *33*(3), 231–248. <https://doi.org/10.1111/jmg.12118>

513 Thomas, J. B., Watson, E. B., Spear, F. S., & Wark, D. A. (2015). TitaniQ recrystallized: experimental confirmation
514 of the original Ti-in-quartz calibrations. *Contributions to Mineralogy and Petrology*.
515 <https://doi.org/10.1007/s00410-015-1120-0>

516 Tomkins, H. S., Powell, R., & Ellis, D. J. (2007). The pressure dependence of the zirconium-in-rutile thermometer.
517 *Journal of Metamorphic Geology*, *25*(6), 703–713. <https://doi.org/10.1111/j.1525-1314.2007.00724.x>

518 Wark, D. A., & Watson, E. B. (2006). TitaniQ: A titanium-in-quartz geothermometer. *Contributions to Mineralogy*
519 *and Petrology*, *152*(6), 743–754. <https://doi.org/10.1007/s00410-006-0132-1>

520 Warren, C. J., Greenwood, L. V., Argles, T. W., Roberts, N. M. W., Parrish, R. R., & Harris, N. B. W. (2019).
521 Garnet-monazite rare earth element relationships in sub-solidus Metapelites: A case study from Bhutan.
522 *Geological Society Special Publication*, *478*(1), 145–166. <https://doi.org/10.1144/SP478.1>

523 Watson, E. B., & Green, T. H. (1981). Apatite/liquid partition coefficients for the rare earth elements and strontium.
524 *Earth and Planetary Science Letters*, *56*(C), 405–421. [https://doi.org/10.1016/0012-821X\(81\)90144-8](https://doi.org/10.1016/0012-821X(81)90144-8)

525 White, R. W., Powell, R., & Clarke, G. L. (2002). The interpretation of reaction textures in Fe-rich metapelite
526 granulites of the Musgrave Block, Central Australia: Constraints from mineral equilibria calculations in the
527 system. *Journal of Metamorphic Geology*, *20*(1), 41–55. <https://doi.org/10.1046/j.0263-4929.2001.00349.x>

528 Yakymchuk, C. (2017). Behaviour of apatite during partial melting of metapelites and consequences for prograde
529 suprasolidus monazite growth. *Lithos*, *274–275*, 412–426. <https://doi.org/10.1016/j.lithos.2017.01.009>

530 Yakymchuk, C., & Brown, M. (2014). Behaviour of zircon and monazite during crustal melting. *Journal of the*

531 *Geological Society*, 171(4), 465–479. <https://doi.org/10.1144/jgs2013-115>

532 Yakymchuk, C., Clark, C., & White, R. W. (2017). Phase Relations, Reactions Sequences and Petrochronology.
533 *Reviews in Mineralogy and Geochemistry*, 83, 15–53. <https://doi.org/10.2138/rmg.2017.83.2>

534 Yakymchuk, C., Rehm, A., Liao, Z., & Cottle, J. M. (2019). Petrochronology of oxidized granulites from southern
535 Peru. *Journal of Metamorphic Geology*, (December 2018), 839–862. <https://doi.org/10.1111/jmg.12501>

536 Zack, T., & Kooijman, E. (2017). Petrology and Geochronology of Rutile. *Reviews in Mineralogy and*
537 *Geochemistry*, 83(1), 443 LP – 467. <https://doi.org/10.2138/rmg.2017.83.14>
538
539

540 **Figure 1.** The most applied interpretations of accessory mineral REE profiles. (a) Schematic illustration of two
541 monazite REE profiles and how they might be interpreted in the context of progressive crystallization during which
542 the abundance of major minerals changes. (b) Example dataset from Rubatto et al. (2006) of monazite core and rim
543 compositions from Mount Stafford, Central Australia. Monazite cores were characterized by low Gd/Lu and high
544 Eu/Eu* compared to monazite rims; this relationship was interpreted to record progressive monazite growth or
545 recrystallization during low-pressure prograde metamorphism as the abundance of alkali-feldspar (preferentially
546 incorporates Eu) and then garnet (preferentially incorporates HREE) increased.

547 **Figure 2.** Phase equilibria of (a) average pelite and (b) greywacke used for the partitioning models of this study
548 (Yakymchuk et al., 2017).

549 **Figure 3.** (A,B) The $\log_{10}fO_2$ of the modeled compositions. (C,D) Differences between $\log_{10}fO_2$ of the modeled
550 compositions and the fayalite–magnetite–quartz buffer (FMQ). The shape of the contours is influenced by reactions
551 among the Fe²⁺–Fe³⁺ minerals—ilmenite, magnetite, garnet, and biotite—most notably the rutile-in reaction with
552 increasing pressure (involving ilmenite breakdown and garnet growth), the magnetite–spinel-in reactions with
553 decreasing pressure, and the biotite-out reaction with increasing temperature. (E,F) The ratio Eu³⁺/Eu^{total} used to
554 calculate Eu partitioning, which was calculated from fO_2 , T , and melt composition (Burnham et al., 2015).

555 **Figure 4.** Calculated equilibrium Eu/Eu* anomalies of accessory minerals and garnet in the MC models: (A,B)
556 zircon, (C,D) monazite, (E,F) apatite, and (G,H) garnet. Accessory mineral and garnet Eu/Eu* are primarily pressure
557 dependent near the solidus, where the accessory minerals are abundant and the relative availability of Eu³⁺ and Eu²⁺
558 is controlled by fO_2 . With increasing temperature, the fraction of each accessory minerals decreases exponentially,
559 particularly monazite, thereby strongly influencing the distribution of REE, resulting in a stronger temperature
560 dependence on Eu/Eu*.

561 **Figure 5.** Calculated equilibrium Eu/Eu* of plagioclase and melt in the MC models: (A,B) plagioclase and (C,D)
562 melt. In contrast to accessory-mineral and garnet Eu/Eu* (Figure 4), feldspar and melt Eu/Eu* are strongly
563 temperature dependent.

564 **Figure 6.** Values of Eu/Eu* in each phase are controlled by the temperature-dependent solubilities of accessory
565 minerals and the pressure-dependent Eu³⁺/Eu^{total} (Figure 3e,f). MC model results along the hypothetical P – T path
566 shown in Figure 4c. Weight percent of phases along the path in (A) pelite and (B) greywacke. Percent of the total Eu
567 in the system hosted by each phase in (C) pelite and (D) greywacke. Values of Eu/Eu* in each phase in (E) pelite
568 and (F) greywacke.

569 **Figure 7.** For the closed-system, equilibrium MC models, accessory mineral Eu anomalies exhibit strong positive
570 correlations Eu³⁺/Eu^{total}, which is primarily a function of pressure (Figure 4), and with monazite stability. In contrast,
571 correlations with the wt% feldspar are inconsistent and variable, illustrating that, at equilibrium, wt% feldspar has
572 minimal influence on accessory mineral Eu/Eu*. (A) Apatite Eu/Eu* as functions of wt% feldspar and temperature
573 at constant pressure. (B) Apatite Eu/Eu* as functions of wt% feldspar and pressure at constant temperature. (C)
574 Apatite Eu/Eu* as functions of whole-rock Eu³⁺/Eu^{total} and temperature at constant pressure. (D) Apatite Eu/Eu* as
575 functions of whole-rock Eu³⁺/Eu^{total} and pressure at constant temperature. In all panels, apatite Eu/Eu* is shown
576 because apatite is stable at all modeled P – T conditions; monazite and zircon show similar Eu/Eu* patterns for the P –
577 T conditions at which they are stable (Figure 4).

578 **Figure 8.** The fractionation of Eu by feldspar growth can decrease Eu/Eu* in accessory minerals and garnet. (A)
579 Weight fractions of plagioclase, alkali-feldspar, and melt in the model metapelite. (B) Weight fractions of
580 plagioclase, alkali-feldspar, and melt in the model greywacke. (C) Effective whole-rock, garnet, and accessory
581 mineral Eu/Eu* for the MC pelite model. The large increase in Eu/Eu* at ~810°C is due to alkali-feldspar resorption
582 during biotite growth. (D) Effective whole-rock, garnet, and accessory mineral Eu/Eu* for the MC greywacke
583 model. Model was ended at 798°C, because the changes in the weight fractions of feldspars are minimal at lower
584 temperature. (E) Effective whole-rock, garnet, and accessory mineral Eu/Eu* for the B94 pelite model. The smaller
585 overall Eu fractionation relative to the MC model is due to lower feldspar $K_d^{Eu^{2+}}$, particularly for the alkali feldspar.
586 (D) Effective whole-rock, garnet, and accessory mineral Eu/Eu* for the B94 greywacke model.

595
596
597
598
599
600
601
602
603
604

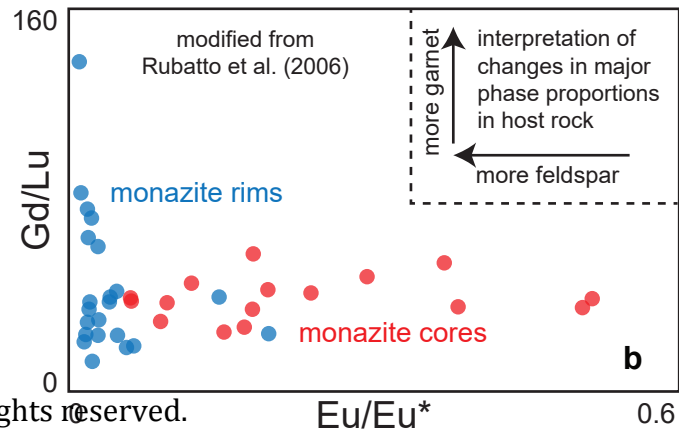
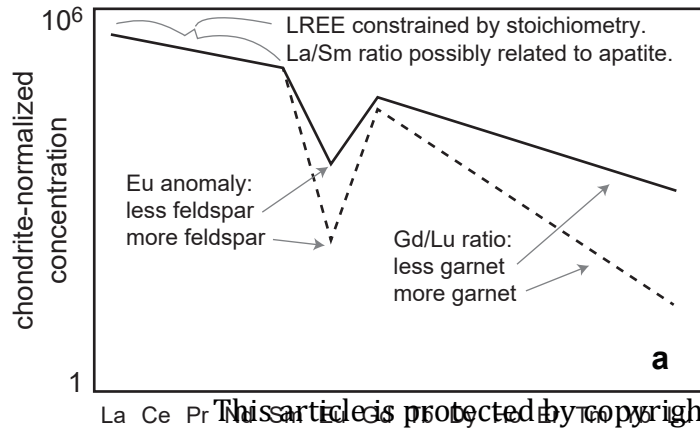
Figure 9. Melt extraction can decrease the effective whole-rock Eu/Eu* and thereby decrease Eu/Eu* of residual minerals; however, the modeled magnitude of this decrease is strongly dependent on the partitioning data used. (A) Weight fractions of plagioclase, alkali-feldspar, melt (remaining in the system), and cumulative extracted melt in the pelite model and (B) in the greywacke model. Whole-rock and mineral Eu/Eu* in the (C) MC pelite model, (D) MC greywacke model, (E) B94 pelite model, and (F) B94 greywacke model. Relative to the MC models, the B94 models show larger draw-down in whole-rock Eu/Eu* by melt extraction, because the melt was calculated to have higher REE concentrations and larger Eu/Eu*.

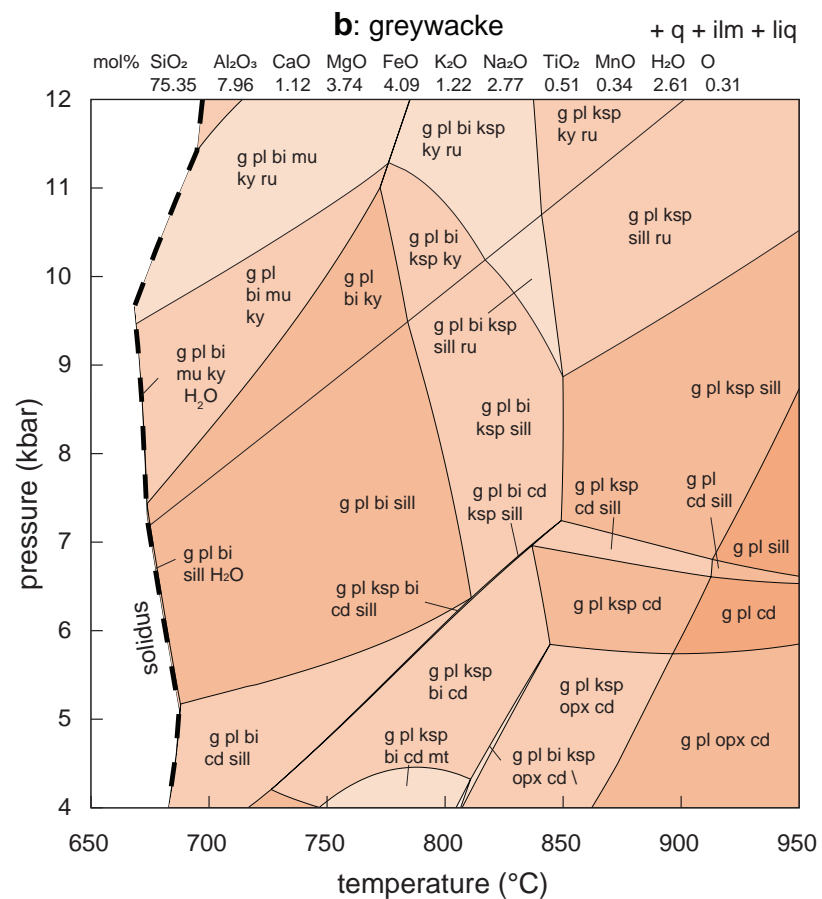
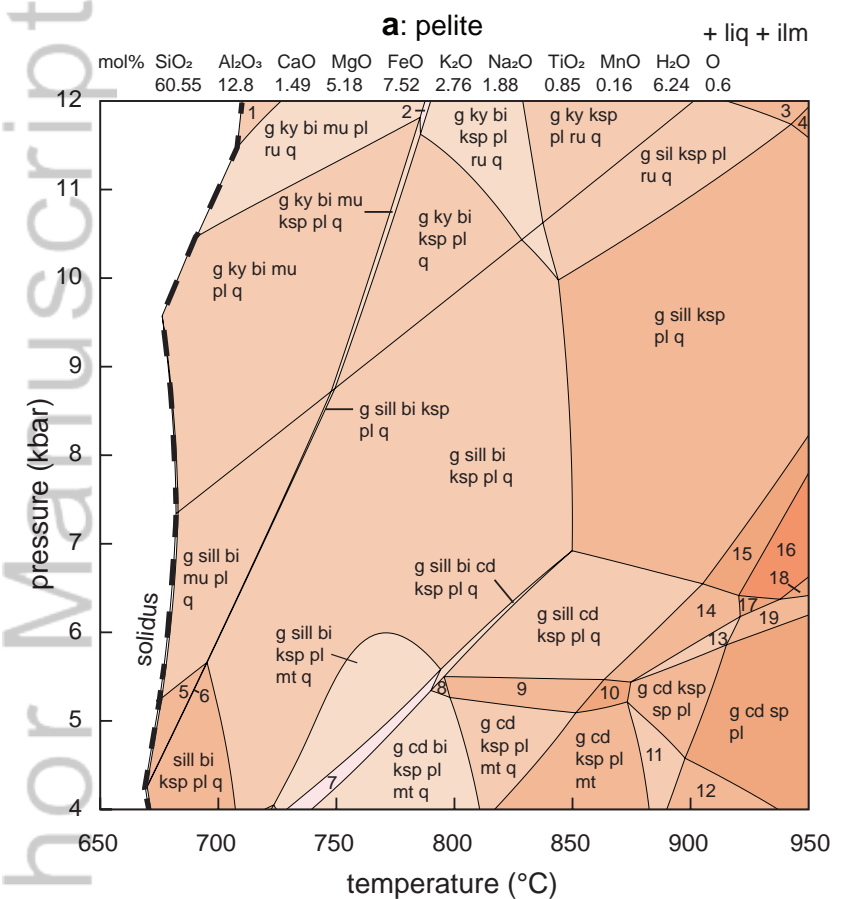
Table 1. Mineral:melt K_d used for Sm, Eu, and Gd partitioning modeling.

Table 1. Mineral:melt K_d used for Sm, Eu, and Gd partitioning modeling

model		monazite	zircon	garnet	apatite	plagioclase
B94	Sm ³⁺	75289	3.79	0.45	1105	1.45
	Eu ²⁺	—	—	0.01	—	1.25
	Eu ³⁺	84934	5.91	1.49	1535	1.72
	Gd ³⁺	95815	9.21	4.95	2133	2.05
Modified-Composite	Sm ³⁺	$50 \cdot 10^{(4373.9/T-1.0034)}$	$10^{(4765.0/T-3.3096)}$	$10^{(5424.0/T-4.1211)}$	$10^{(4037.9/T-1.7169)}$	$0.1 \cdot K_d^{Eu2+}$
	Eu ²⁺	$10^{(4317.3/T-3.8397)}$	$10^{(4838.2/T-5.4992)}$	$10^{(4266.1/T-5.0498)}$	$10^{(-738.33/T+0.9258)}$	Sun et al. (2017)
	Eu ³⁺	$50 \cdot 10^{(4317.3/T-1.0125)}$	$10^{(4838.2/T-3.1581)}$	$10^{(4266.1/T-2.8259)}$	$10^{(4359.3/T-1.9877)}$	$0.1 \cdot K_d^{Eu2+}$
	Gd ³⁺	$50 \cdot 10^{(4254.2/T-1.0158)}$	$10^{(5147.7/T-3.2562)}$	$10^{(3470.9/T-1.8673)}$	$10^{(4670.0/T-2.2498)}$	$0.1 \cdot K_d^{Eu2+}$

605





1: g bi mu pl ru q
 2: g ky bi mu ksp pl ru q
 3: g sill ksp ru q
 4: g sill ksp q

5: sill bi mu pl q
 6: sill ksp bi mu pl q
 7: g sill cd bi ksp pl mt q
 8: g sill bi ksp pl mt q

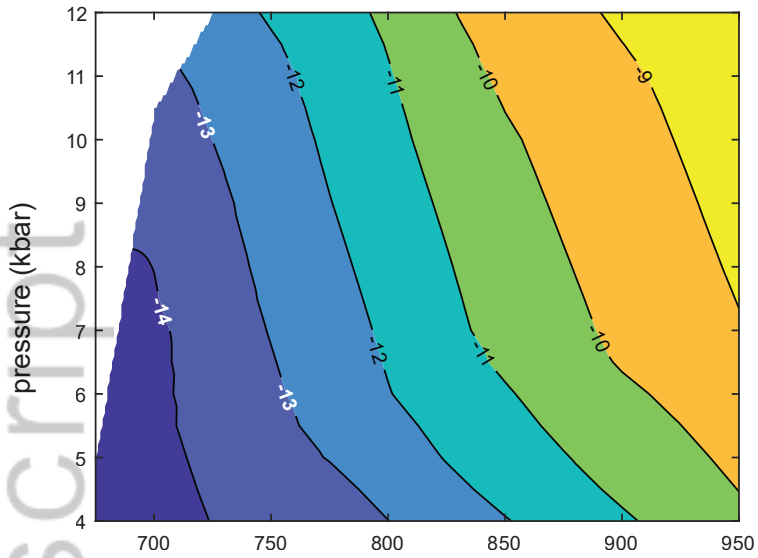
9: g cd ksp pl q
 10: g cd ksp pl
 11: g cd ksp sp pl mt
 12: g cd sp pl

13: g sill cd ksp sp pl
 14: g sill cd ksp pl
 15: g sill ksp pl
 16: g sill ksp pl q

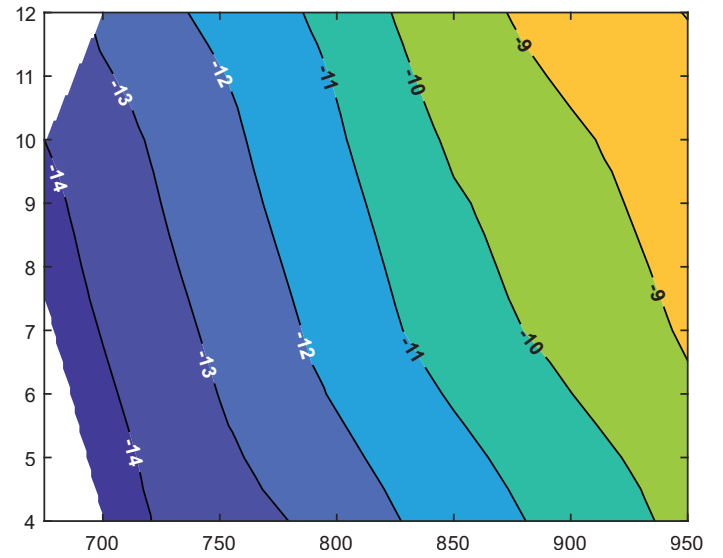
17: g sill cd pl
 18: g sill sp pl
 19: g sill cd sp pl

This article is protected by copyright. All rights reserved.

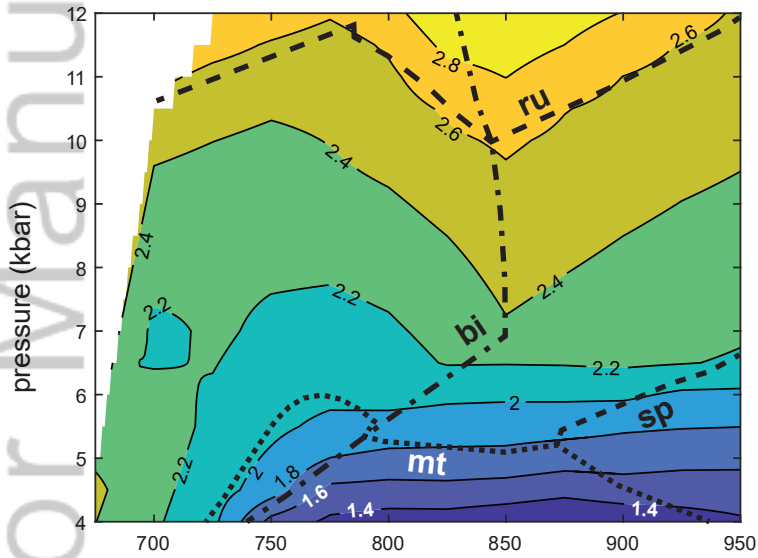
a: $\log_{10}(fO_2 \text{ rock})$, pelite



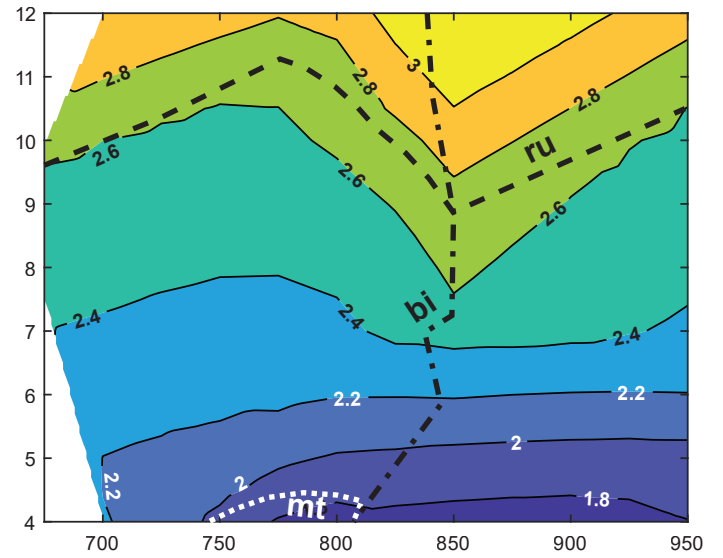
b: $\log_{10}(fO_2 \text{ rock})$, greywacke



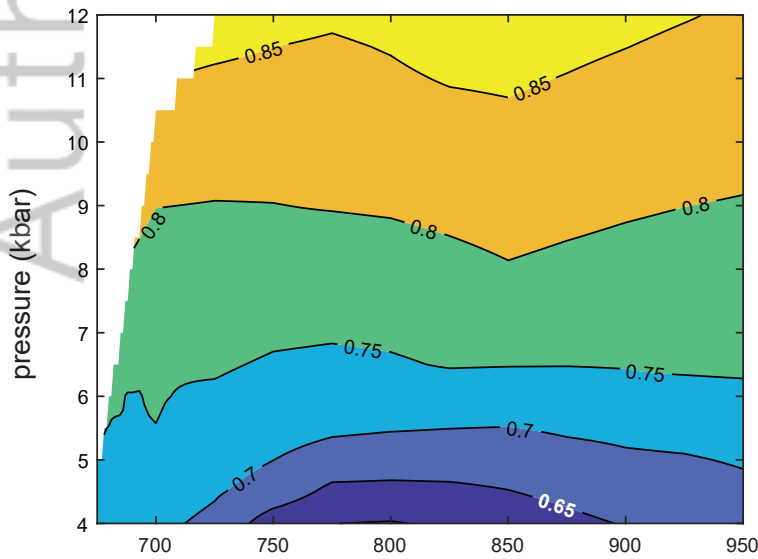
c: $\log_{10}(fO_2 \text{ rock}) - \log_{10}(fO_2 \text{ FMQ})$, pelite



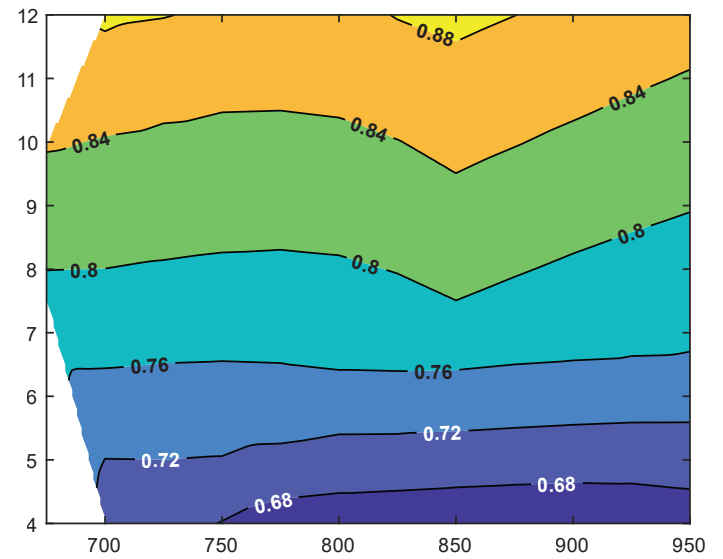
d: $\log_{10}(fO_2 \text{ rock}) - \log_{10}(fO_2 \text{ FMQ})$, greywacke

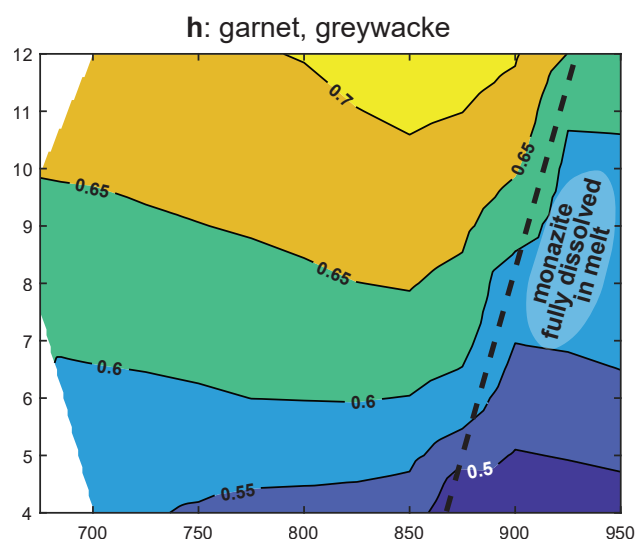
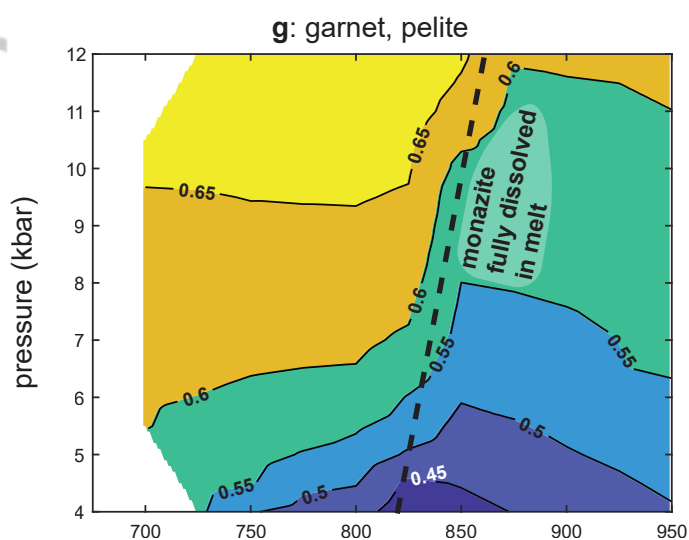
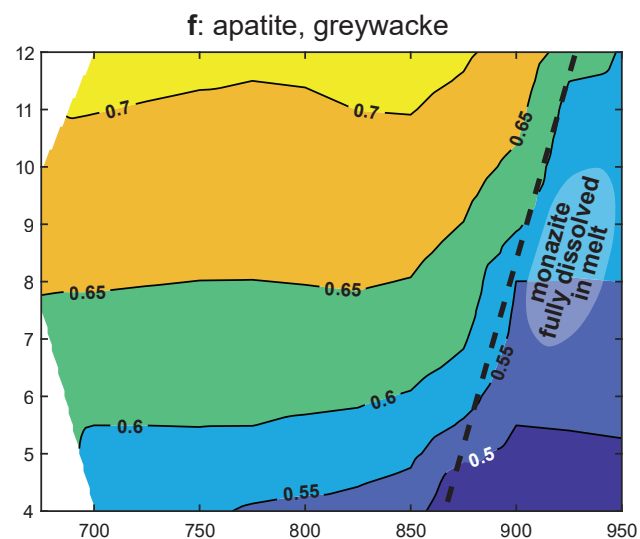
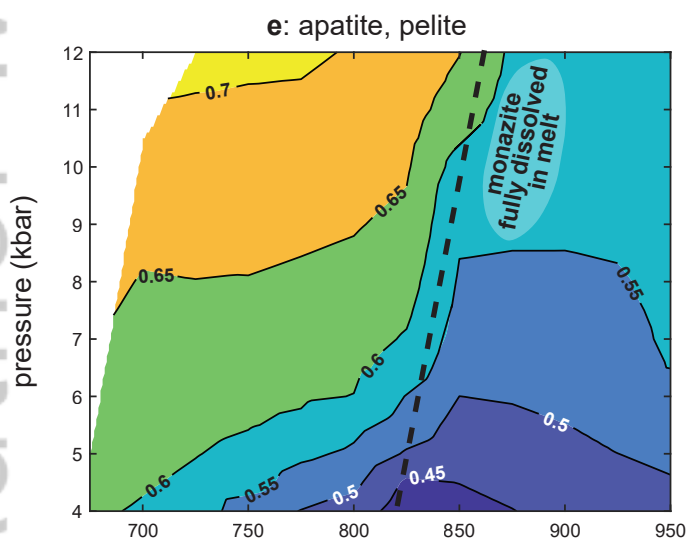
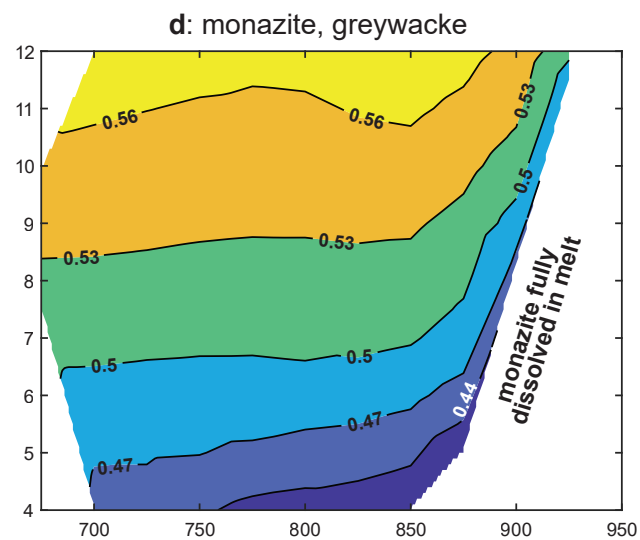
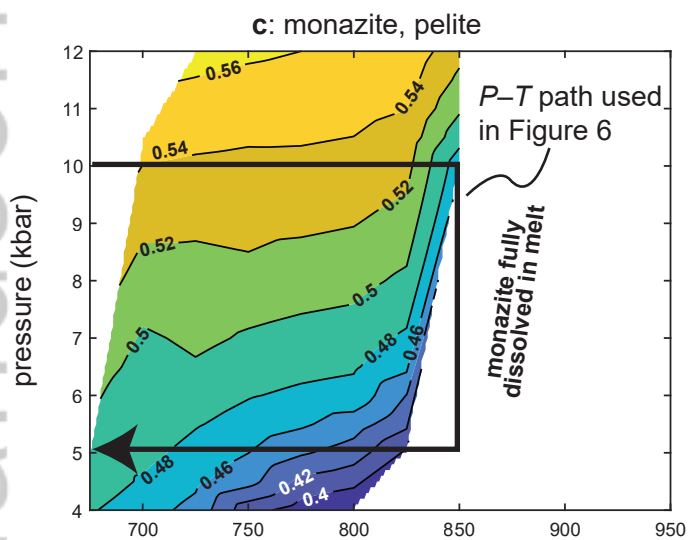
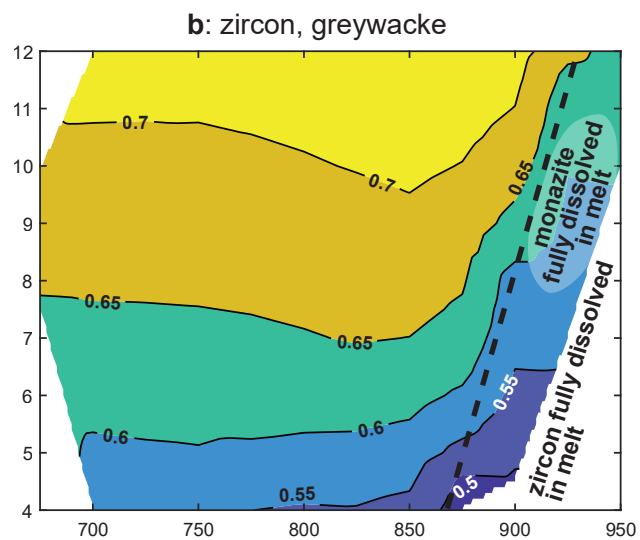
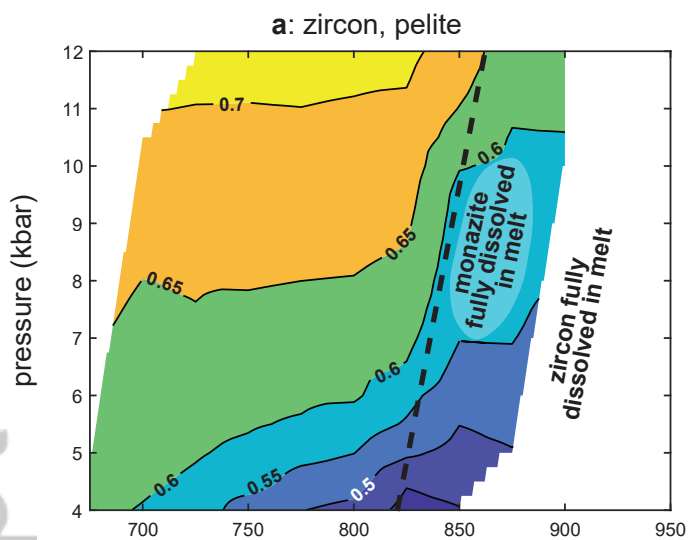


e: Eu^{3+}/Eu^{total} , pelite

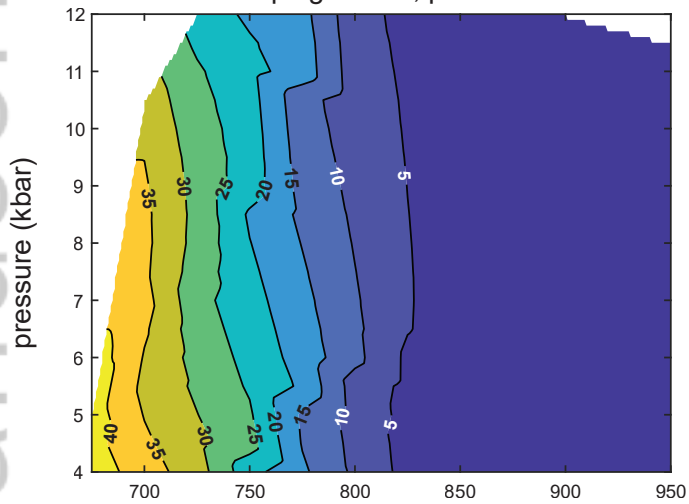


f: Eu^{3+}/Eu^{total} , greywacke

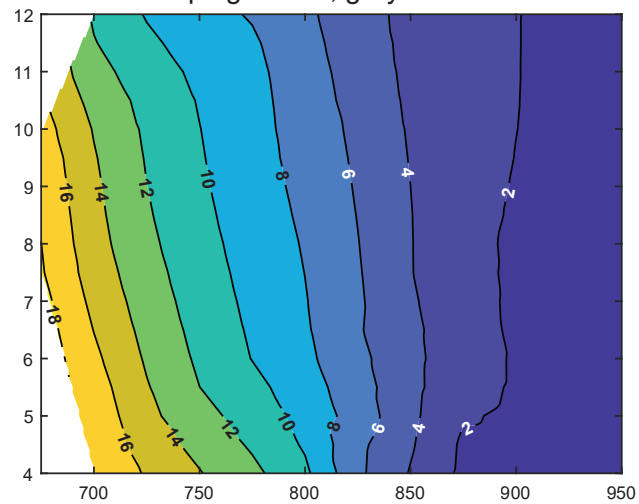




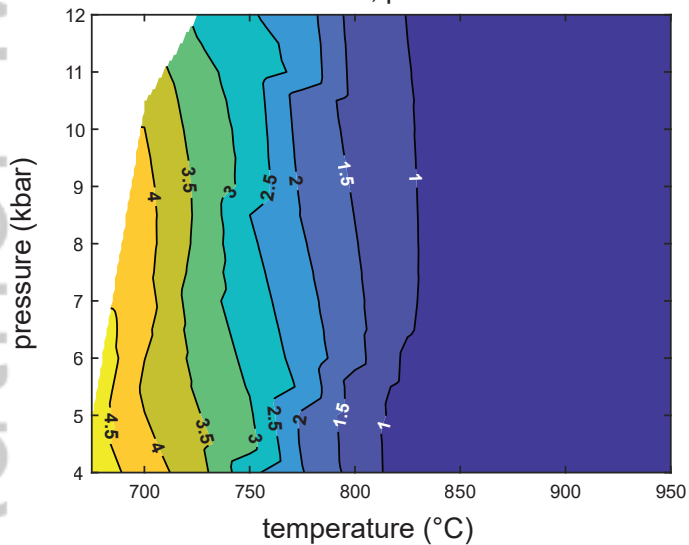
a: plagioclase, pelite



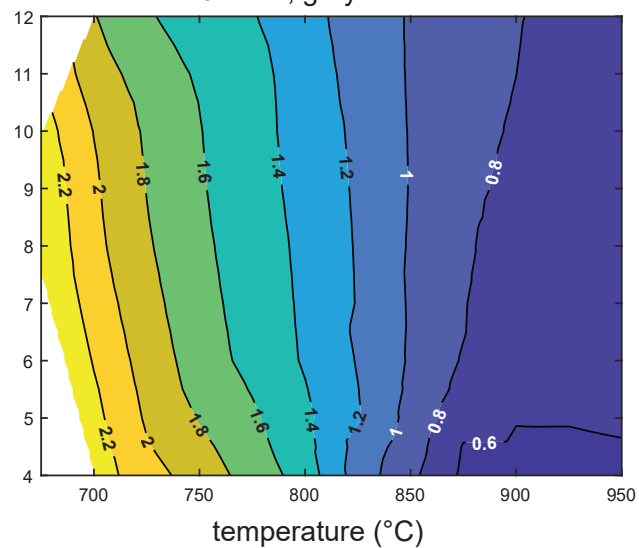
b: plagioclase, greywacke

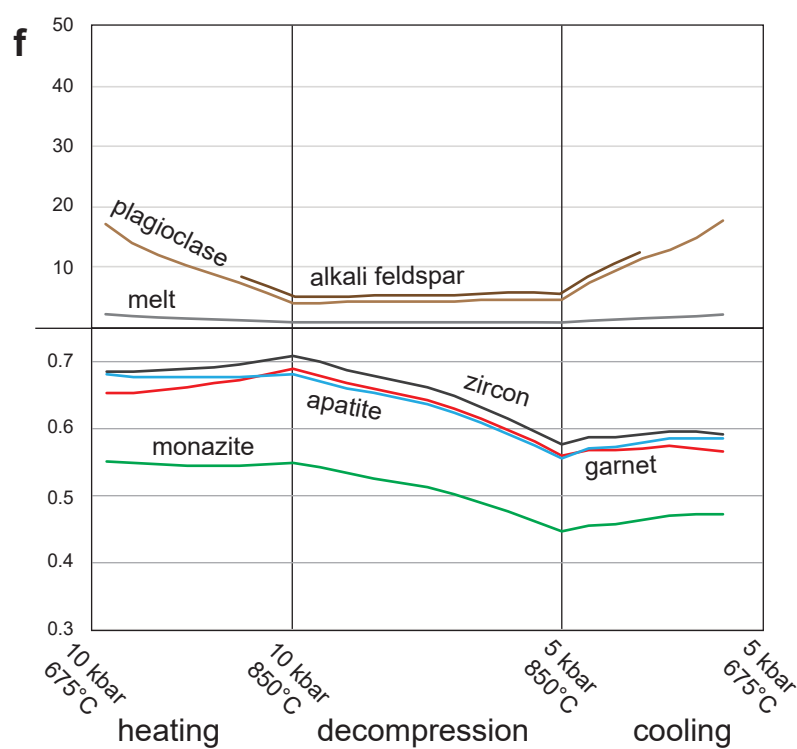
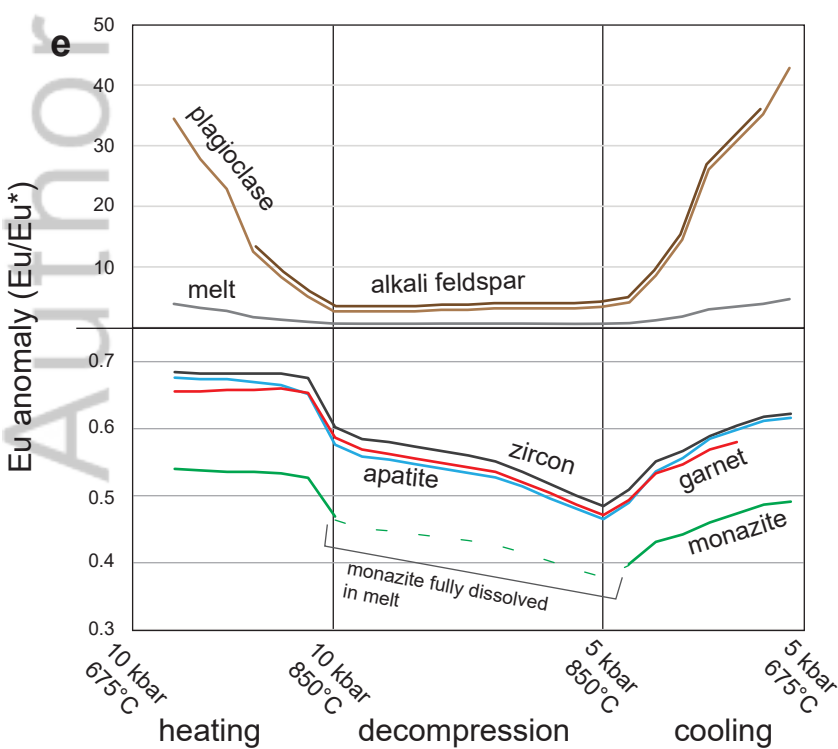
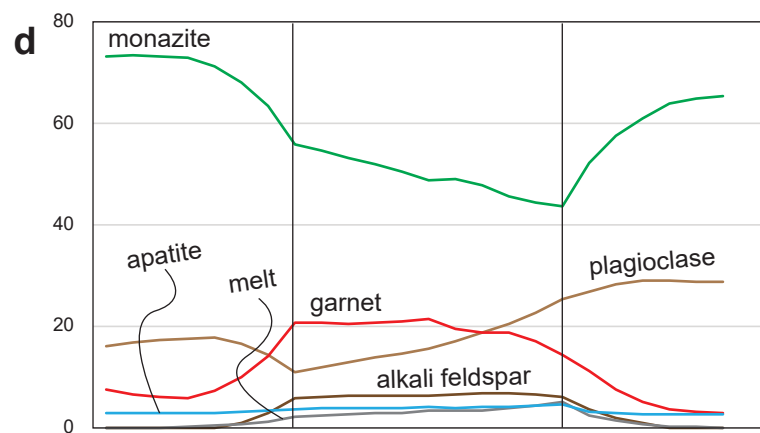
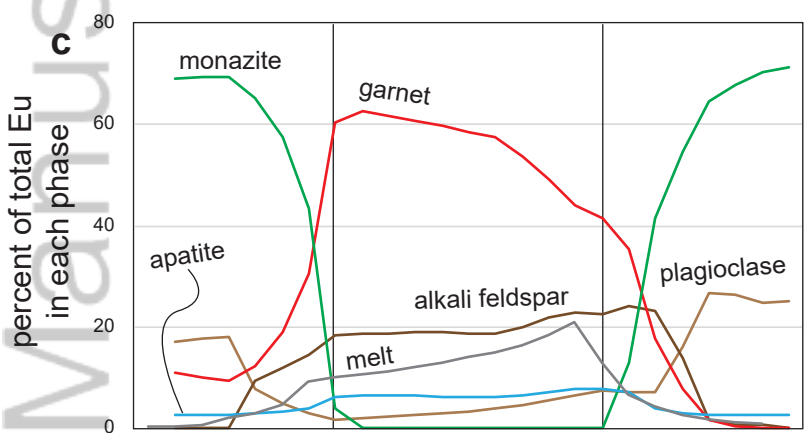
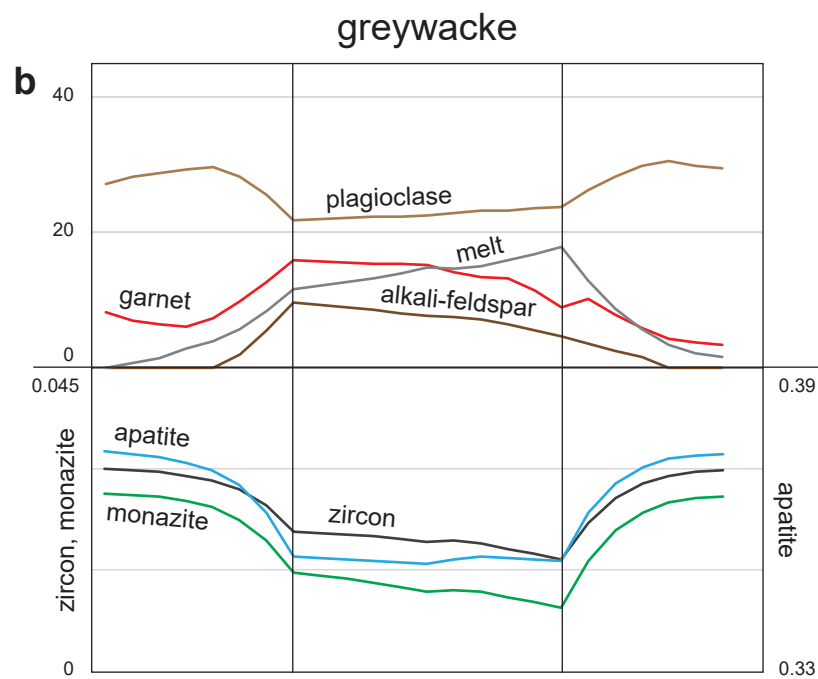
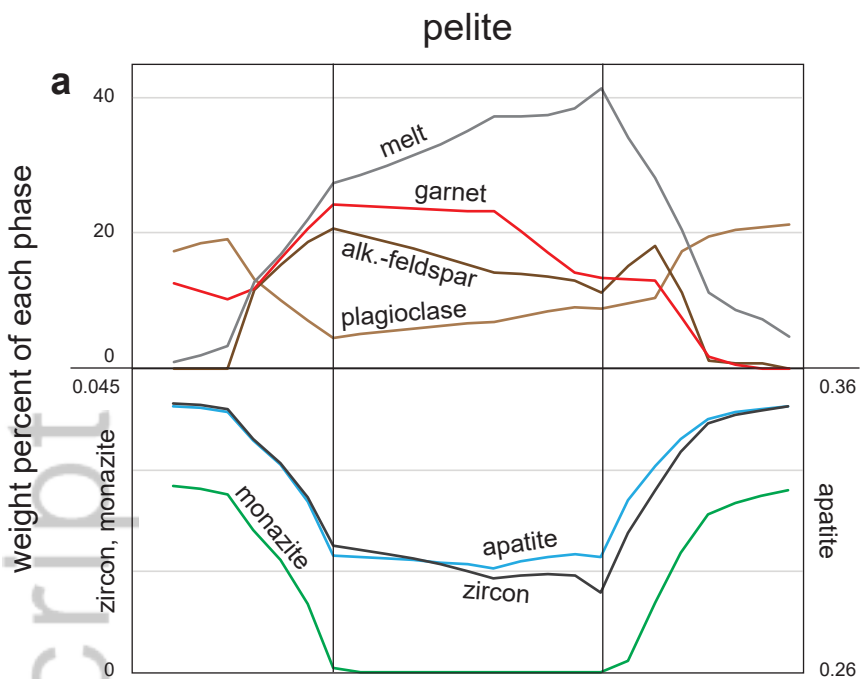


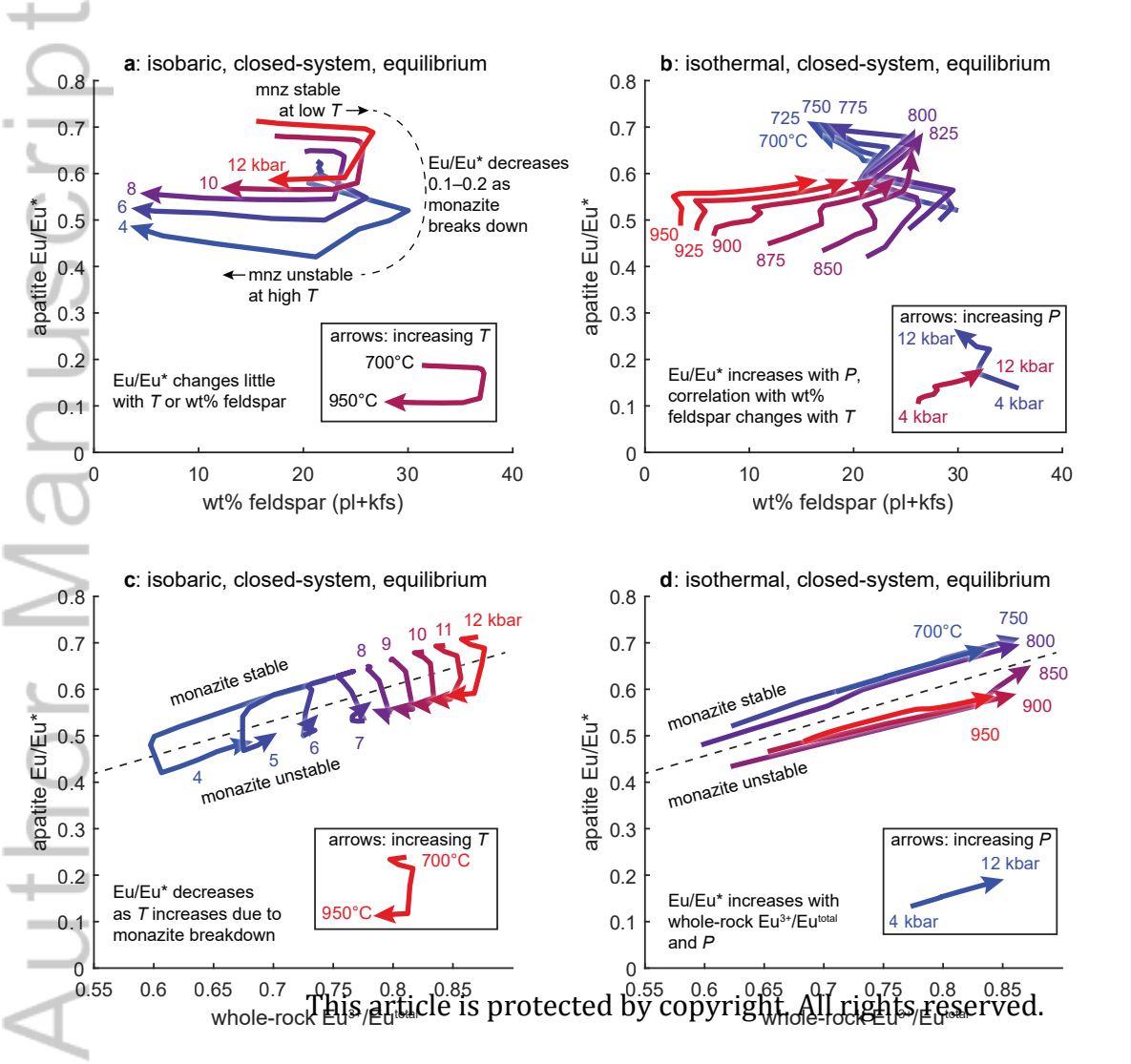
c: melt, pelite



d: melt, greywacke

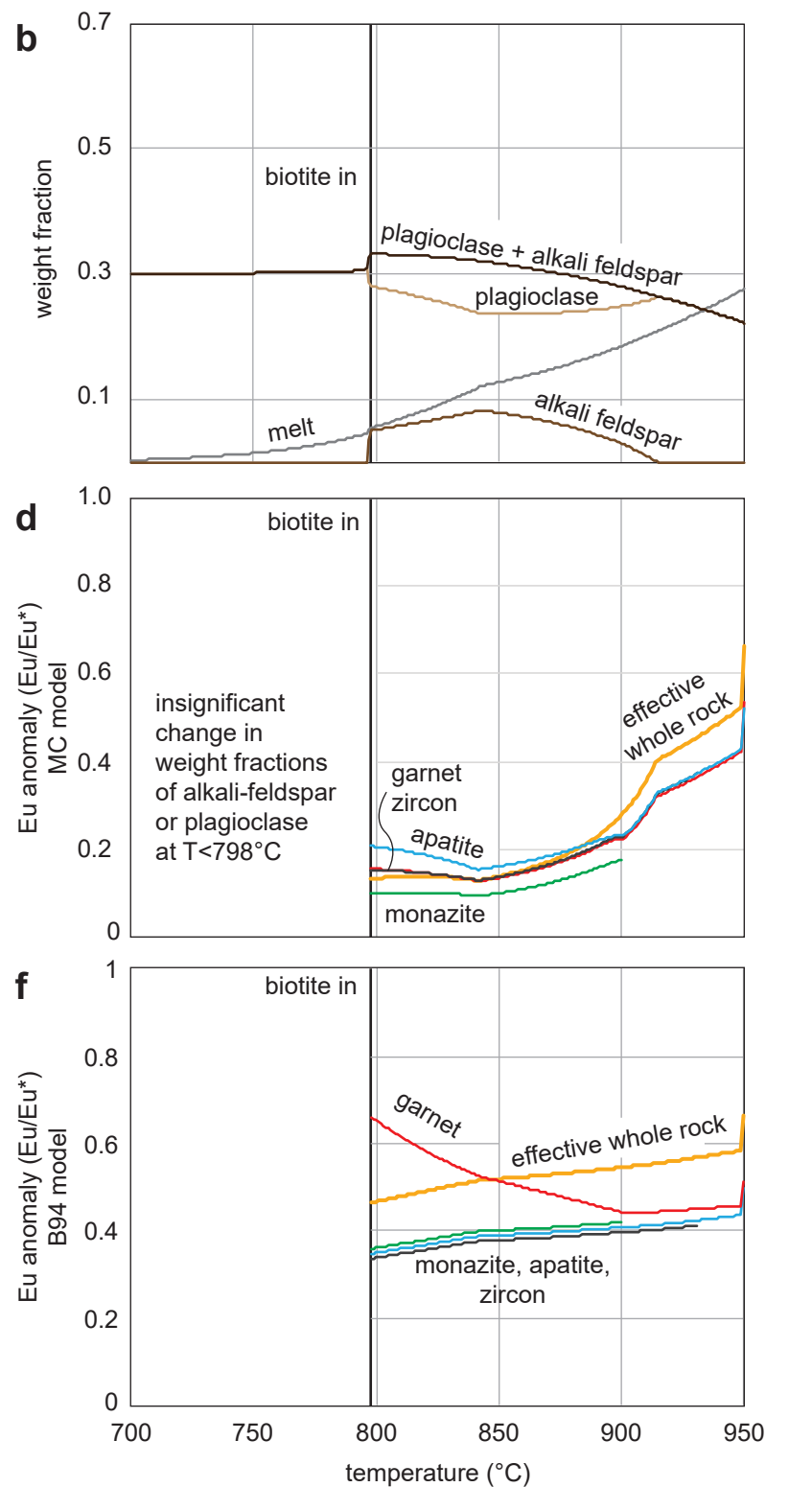
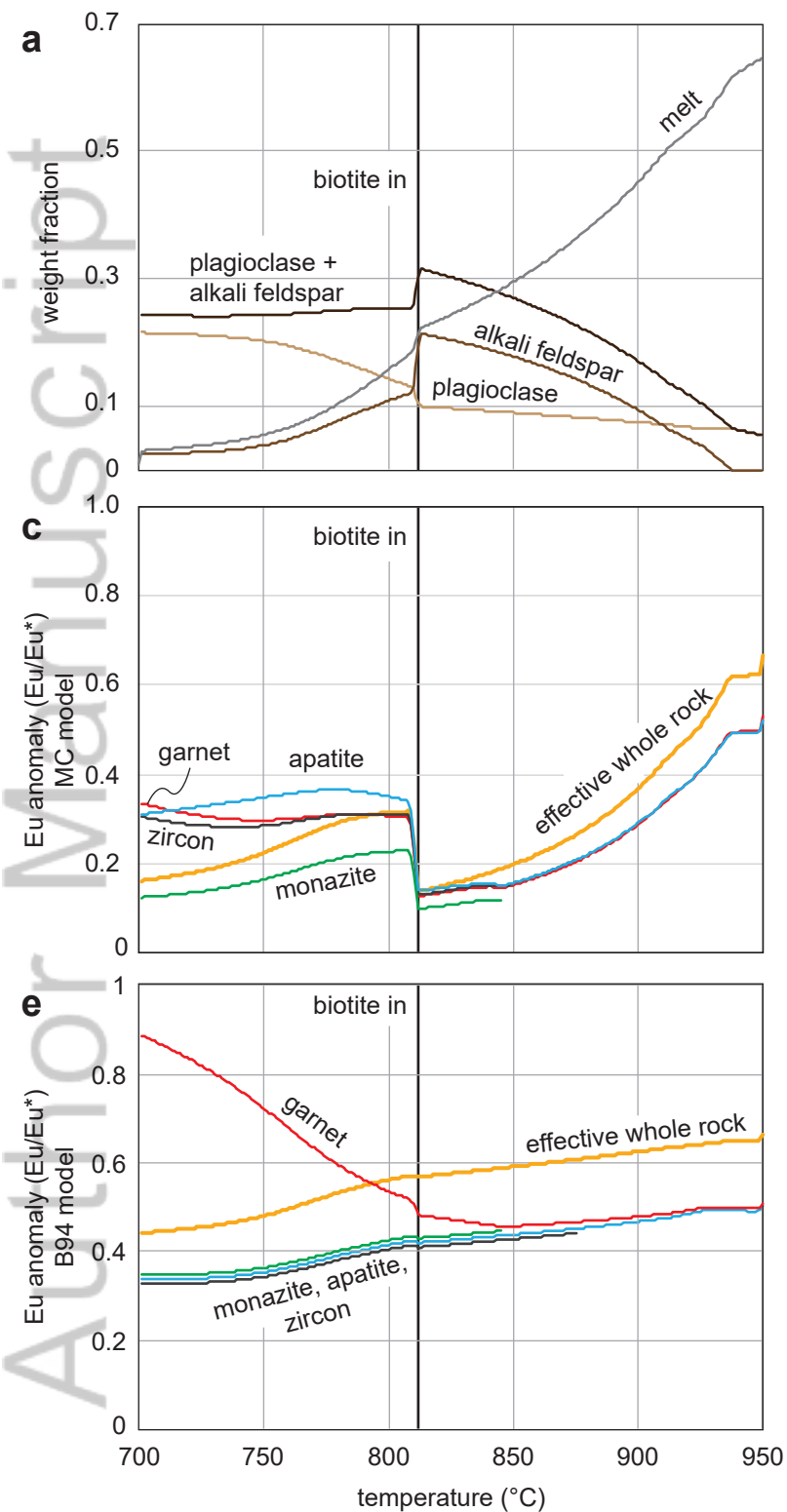






pelite

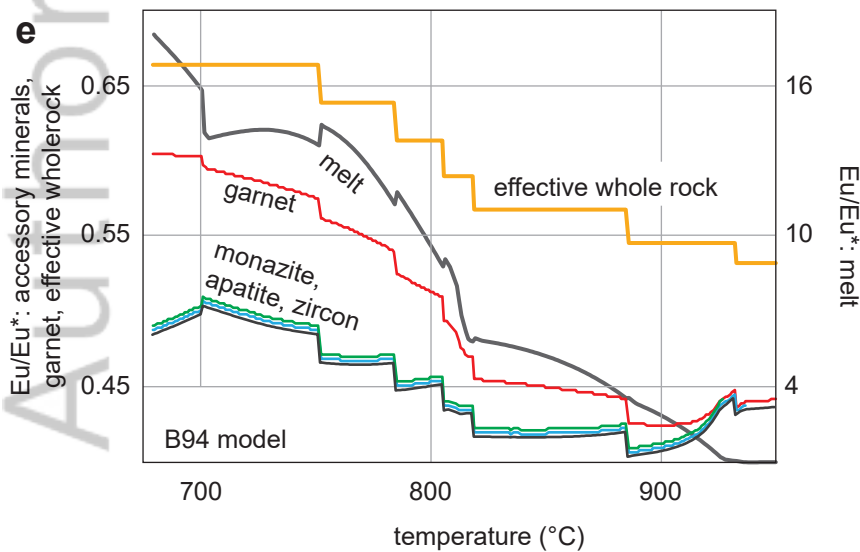
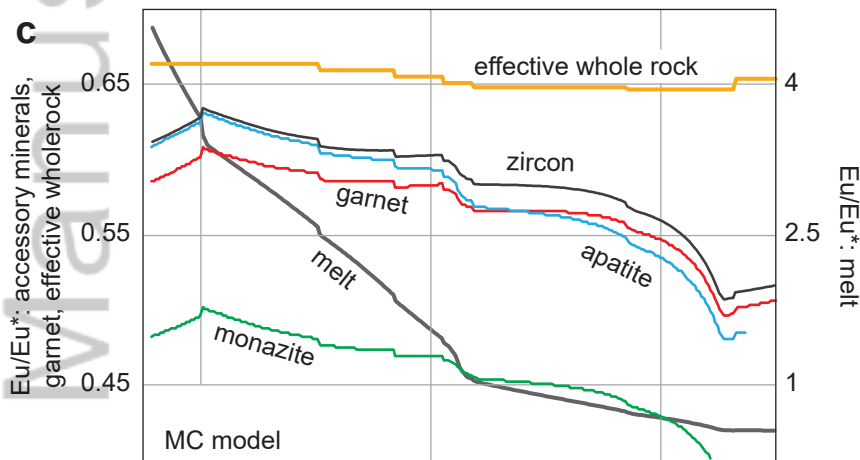
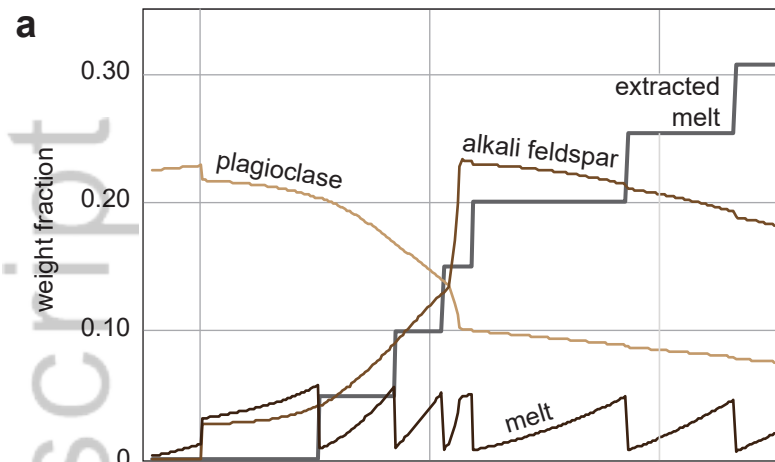
greywacke



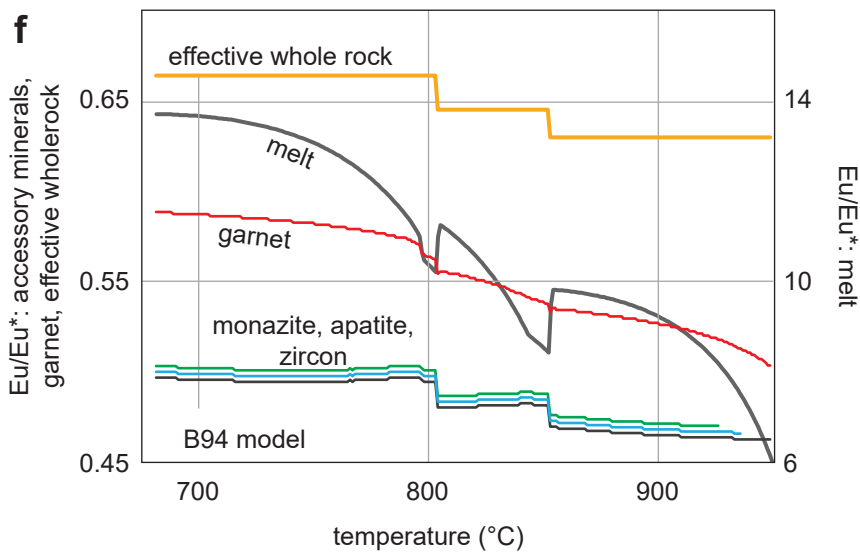
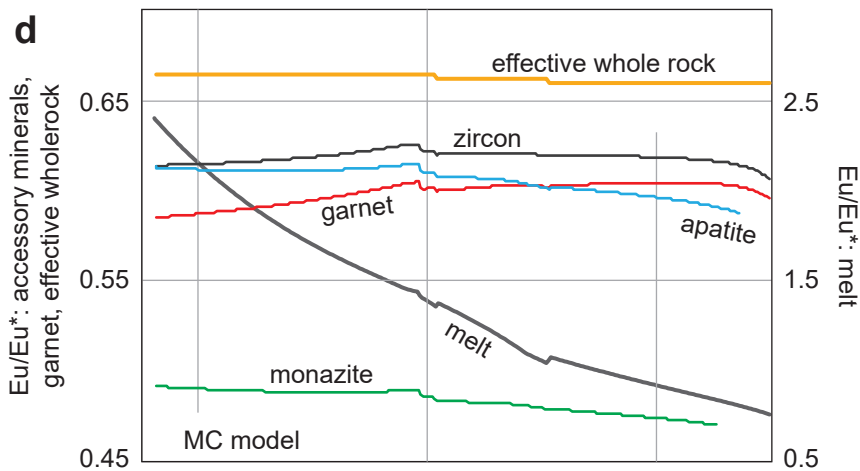
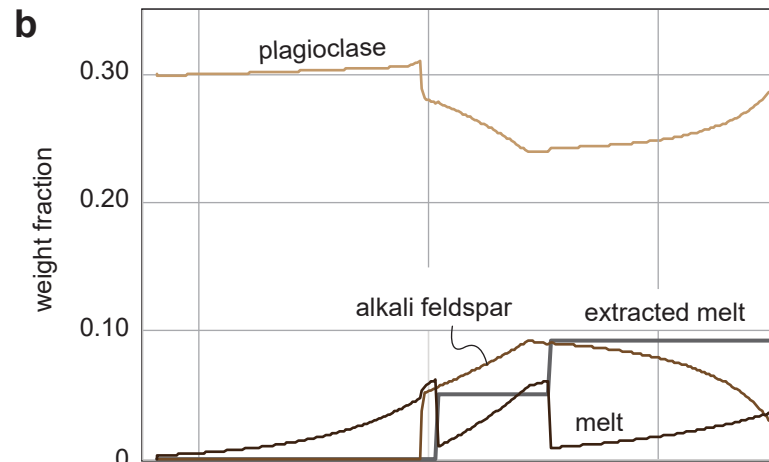
← feldspar fractionation of REE during isobaric cooling

← feldspar fractionation of REE during isobaric cooling

pelite



greywacke



batch melt extraction during isobaric heating →

batch melt extraction during isobaric heating →